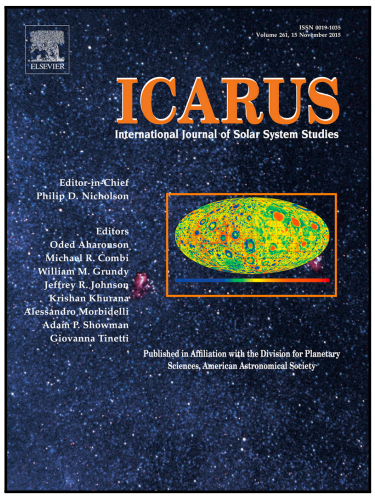

Copper enrichments in the Kimberley formation in Gale crater, Mars: Evidence for a Cu deposit at the source

Valérie Payré , Cécile Fabre , Violaine Sautter , Agnès Cousin , Nicolas Mangold , Laetitia Le Deit , Olivier Forni , Walter Goetz , Roger C. Wiens , Olivier Gasnault , Pierre-Yves Meslin , Jérémie Lasue , William Rapin , Ben Clark , Marion Nachon , Nina L. Lanza , Sylvestre Maurice

PII: S0019-1035(18)30477-9
DOI: https://doi.org/10.1016/j.icarus.2018.12.015
Reference: YICAR 13131

To appear in: *Icarus*

Received date: 13 July 2018
Revised date: 5 December 2018
Accepted date: 5 December 2018

Please cite this article as: Valérie Payré , Cécile Fabre , Violaine Sautter , Agnès Cousin , Nicolas Mangold , Laetitia Le Deit , Olivier Forni , Walter Goetz , Roger C. Wiens , Olivier Gasnault , Pierre-Yves Meslin , Jérémie Lasue , William Rapin , Ben Clark , Marion Nachon , Nina L. Lanza , Sylvestre Maurice , Copper enrichments in the Kimberley formation in Gale crater, Mars: Evidence for a Cu deposit at the source, *Icarus* (2018), doi: https://doi.org/10.1016/j.icarus.2018.12.015

Highlights

- Quantification of copper using Laser Induced Breakdown Spectroscopy (LIBS)
- Copper occurrence in fractures, potentially related to adsorption on Mn-oxides
- Copper in sedimentary units suggesting upstream hydrothermal processes that formed a Cu-deposit

Copper enrichments in the Kimberley formation in Gale crater, Mars: Evidence for a Cu deposit at the source

Valérie Payré[a] (vpayre@rice.edu), Cécile Fabre[b], Violaine Sautter[c], Agnès Cousin[d], Nicolas Mangold[e], Laetitia Le Deit[e], Olivier Forni[d], Walter Goetz[f], Roger C. Wiens[g], Olivier Gasnault[d], Pierre-Yves Meslin[d], Jérémie Lasue[d], William Rapin[h], Ben Clark[i], Marion Nachon[j], Nina L. Lanza[g], Sylvestre Maurice[d].

[a] Rice University, 6100 Main Street, Houston, TX 77005, USA

[b] GeoRessources, Université de Lorraine, 1 Boulevard des Aiguillettes, 54500 Vandoeuvre-lès-Nancy, France

[c] Muséum National des Histoires Naturelles (MNHN), 57 rue cuvier, 75005 Paris, France

[d] Institut de Recherche en Astrophysiques et Planétologie (IRAP), 9 avenue du colonel roche, 31400 Toulouse, France

[e] Laboratoire de Planétologie et Géodynamique, 2 rue de la houssinière, 44322 Nantes Cédex 3, France

[f] Max Planck Institut für Sonnensystemforschung, Justus-von-Liebig-Weg 3, 37077 Göttingen, Germany

[g] Los Alamos National Laboratory (LANL), Los Alamos, NM 87545, USA

[h] California Institute of Technology, 200 E California Blvd, Pasadena, CA 91125, USA

[i] Space Science Institute, 4750 Walnut St, Suite 205, Boulder, CO 80301, USA

[j] University of California, Davis, 1 Shields Ave, Davis, CA 95616, USA

vpayre@rice.edu; cecile.fabre@univ-lorraine.fr; violaine.sautter@mnhn.fr; Agnes.Cousin@irap.omp.eu; nicolas.mangold@univ-nantes.fr; laetitia.ledeit@univ-nantes.fr;

Olivier.Forni@irap.omp.eu; goetz@mps.mpg.de; rwiens@lanl.gov;

Olivier.Gasnault@irap.omp.eu; pmeslin@irap.omp.eu; jlasue@irap.omp.eu;

wrapin@caltech.edu; bclark@SpaceScience.org; mnachon@ucdavis.edu; nlanza@lanl.gov;

sylvestre.maurice@irap.omp.eu .

Corresponding author: vpayre@rice.edu

Phone number corresponding author: +17029573197

Abstract

Copper quantification with laser induced breakdown spectroscopy (LIBS) using a univariate calibration model enables the ChemCam instrument onboard the Curiosity rover to measure unusually elevated Cu concentrations in potassic sandstones and Mn-oxide-bearing fracture fills in the Kimberley region of Gale crater, Mars. Mostly, the copper phases occurring in sedimentary bedrock are associated with detrital silicates, including feldspars, pyroxenes and K-phyllosilicates, likely coming from a potassic igneous source near the northern crater rim, while those present in the fractures are likely adsorbed on the surface of manganese oxides. These two different mineralogical associations imply at least two distinct processes: Cu enrichment in bedrock at the source, likely during crystallization of the igneous silicates, and adsorption of Cu on Mn-oxides precipitated from groundwater that encountered oxidizing conditions within fractures in the bedrock. The potassic sediments enriched in copper may be evidence of a porphyry copper deposit or an impact-induced hydrothermal deposit in the source region.

Keywords

Copper deposit, Gale crater, Kimberley, ChemCam, hydrothermal alteration

1 Introduction

The surface of Mars is particularly sulfur rich in comparison with the terrestrial crust, for which the average sulfur content is estimated around 620 ppm (Rudnick and Gao, 2003): the global Martian map of S distribution determined by the Mars Odyssey gamma-ray spectrometer (Karunatillake et al., 2014), which has a relatively large footprint revealed S values up to 3.0 wt. % (SO_3 = 7.5 wt. %), with an average of S = 1.8 wt. % (SO_3 = 4.4 wt. %) in the tens of centimeters below the surface (McLennan et al., 2010). Thermal and infrared observations from orbit indicate large secondary deposits of sulfate minerals such as gypsum dunes (Langevin et al., 2005). *In situ* analyses have shown several classes of rocks at Columbia Hills (e.g., Ming et al., 2006; Squyres et al., 2006) that are rich in sulfates. Rover-based analyses also reveal that calcium sulfate is ubiquitous in fracture-fills, observed at Opportunity and Curiosity landing locations including Endeavour crater and Gale crater respectively (Arvidson et al., 2014; Nachon et al., 2014), and indicating S-rich groundwater. Soil contains relatively elevated S concentrations, with an average amount of SO_3 around 6 wt. % (Hahn and McLennan, 2007), with some soils containing up to 32 wt. % as SO_3 (Paso Robles; Ming et al., 2006). A conservative estimate of total surficial SO_3 in Martian soil sedimentary deposits and polar sulfates comprises about 7.5 x 10^{16} kg (Righter et al., 2009). As a result, by analogy with terrestrial geochemical processes, the Martian surface would be expected to show elevated concentrations of chalcophile elements such as zinc and copper, two transition elements typically associated with sulfur to form sulfides.

The average content of zinc in Martian soil calculated from the in situ Spirit and Opportunity rovers' measurements is 286 ppm (Hahn and McLennan, 2007), and its abundance varies in sediments: the Alpha Particle X-ray Spectrometer (APXS) instrument from the Mars Exploration Rovers missions have measured values ranging from 40 to 2300 ppm (http://pds-geosciences.wustl.edu). As a whole, Zn content in the Martian crust is estimated to be four

times higher than in the terrestrial crust (80 ppm), with Mars abundances of 320 ppm (McLennan, 2001; Taylor and McLennan, 2009). In addition, APXS and the Chemistry and Camera instrument (ChemCam) onboard the Mars Science Laboratory (MSL) mission Curiosity rover measured ZnO concentrations up to ~8 wt. % in Gale crater (Lasue et al., 2016; Thompson et al., 2016).

Concerning copper, among all Mars missions, the MSL mission is the first able to report and quantify Cu abundances. The APXS instrument has detected values up to 580 ppm within a sedimentary bedrock named Liga in Gale crater (Berger et al., 2017). In martian meteorites, the bulk Cu value obtained does not exceed 23 ppm, i.e., largely lower than the mean terrestrial mid-ocean ridge basalt composition of 81 ppm (White and Klein, 2014). This is thought to reflect a lower budget of Cu in the Martian mantle: Mars being a smaller planet compared to the Earth, its core formed at lower pressure and Cu became more siderophile, likely concentrating more in the core (Wang and Becker, 2017). Therefore, the copper concentration in Mars' mantle is suggested to be 15 times lower than the terrestrial mantle with an estimated value of 2 ppm (Wang and Becker, 2017). However, the elevated copper contents analyzed by APXS in Gale crater suggest that Cu-bearing minerals should be present at the surface of Mars. Moreover, in the martian meteorites, the main form of Cu minerals is chalcopyrite ($CuFeS_2$), commonly found in association with pyrrhotites in shergottites, within glasses in Chassigny, and within the mesostasis of Nakhla along with plagioclases and alkali feldspars (Boctor et al., 1976; Bunch and Reid, 1975; Lorand et al., 2005; McSween, 1994; Rochette et al., 2001). On Earth, Cu-bearing massive sulfide deposits, which are important sources of copper, usually contain abundant chalcopyrite along with other sulfides like pyrite and sphalerite (Shanks and Thurston, 2012; Slack et al., 2003). The most considerable chalcopyrite-bearing deposits have a hydrothermal origin, such as the largest Canadian chalcopyrite deposit in the Temagami Greenstone Belt (Baknes, 1990). Regarding the

detection of these elements in martian materials and the occurrence of hydrothermal circulation on Mars (e.g., (Berger et al., 2017)), discovering such Cu-Zn deposits should be plausible even if martian crustal copper is much less abundant than on Earth.

Although ChemCam is able to detect copper, no quantification has been done yet (Maurice et al., 2012; Wiens et al., 2012, 2013). In this study, we report the first detections and quantifications of martian copper abundances using ChemCam data. Since Curiosity's payload measured elevated copper abundances at Kimberley (4.64°N, 137.4°E) in comparison with other regions of Gale crater, this study focuses on this area (Stack et al., 2016). We describe plausible Cu mineralogical associations within Cu-rich materials and then discuss their potential origin according to the Kimberley geological context.

2 Geological context and composition of the Kimberley formation

The MSL rover landed on the 6th of August 2012 in Gale Crater at the Bradbury landing site that is close to an alluvial fan lobe (Grotzinger et al., 2015). An apparent fluvial channel associated with the fan crosses the northwestern Gale crater rim (Grotzinger et al., 2015; Palucis et al., 2014). Curiosity encountered clastic sedimentary rocks in the Yellowknife Bay formation (Sols 53 - 340), and after a traverse of several kilometers, arrived at the potassic- and iron-rich sandstone region named Kimberley (Sols 576 – 632). After that, the rover traveled up to the base of Aeolis Mons, reaching the Murray (circa Sol 750) and the Stimson formations at the base of Aeolis Mons, which respectively have been interpreted as a former lacustrine and a former aeolian environment (Banham et al., 2018; Grotzinger et al., 2015).

The Kimberley region is stratigraphically above the outcrops encountered earlier at Yellowknife Bay (Grotzinger et al., 2015; Stack et al., 2016). It includes six geological

members, as shown in the High Resolution Imaging Science Experiment (HiRISE) orbital image and the stratigraphic column in Figure 1a-b. In the ascending stratigraphic order, there are: the conglomerate Point Coulomb member; the Liga member presenting poorly sorted conglomerate and centimeter-thick beds (Figure 2a); the Square Top member showing thick coarse-grained sandstone bedsets (Figure 2b); the Dillinger member consisting of medium to fine-grained sandstones crosscut by fracture-fills with low angles (Figure 3a); the Mount Remarkable member corresponding to massive coarse sandstones (Figure 3a); and the Beagle member consisting of dark sandstones that cap Mount Remarkable and other hills of Kimberley (Figure 3b) (Le Deit et al., 2016). The Liga member has been analyzed at four distinct sites by ChemCam: the northern site (Figure 2b), the eastern site, the southern site, and the site south of Kimberley (Figure 2a).

According to APXS and ChemCam measurements, the major and minor/trace elemental compositions observed at Kimberley clearly differ from all other areas in Gale crater. They contain strikingly elevated concentrations of potassium with an average of K_2O ~ 2.5 wt. % in comparison with the Martian crust having an average of K_2O ~ 0.45 wt. % (Le Deit et al., 2016; Taylor and McLennan, 2009). This is in agreement with K-feldspars and K-bearing clays detected by X-ray diffraction from the CheMin instrument within the sandstone named Windjana located in the Dillinger member shown in Figure 3b (Treiman et al., 2016). Based on the chemical composition, minerals analyzed within the Windjana sample appear similar to those present in materials from other Kimberley members (Treiman et al., 2016). These minerals are thought to be detrital, and potassic minerals are thought to come from K-rich igneous rocks such as trachyte or the alkaline igneous rocks described by Sautter et al. (2015) and Cousin et al. (2017). In addition, anomalously high minor and trace element contents (Mn, Cu, Zn, Li, Sr, Rb, Ni, F, Ge and Br) have been measured at Kimberley by both APXS and ChemCam (Berger et al., 2017; Olivier Forni et al., 2015; Gellert et al., 2014; Lanza et

al., 2016; Lasue et al., 2016; Payré et al., 2017). Indeed, the most elevated copper value measured by APXS in Gale crater was found in the target Liga, after which the Liga member is named; it contains 580 ± 10 ppm Cu, i.e. ~ 300 times higher than in the martian mantle (Berger et al., 2017; Thompson et al., 2016; Wang and Becker, 2017). In the Kimberley region, ChemCam acquired more than 600 points of chemical analyses, and some of them displayed anomalous intense emission peaks which were identified as copper lines (Goetz et al., 2017). To address this ChemCam data, we developed a copper calibration curve based on a univariate model of the Cu LIBS emission lines (see details supplementary material).

3 Methodology: Copper quantification with ChemCam

The ChemCam suite consists on a laser induced breakdown spectrometer (LIBS) that is able to detect and analyze major, minor, and trace element compositions (Maurice et al., 2012, 2016, Wiens et al., 2012, 2015), and a remote micro-imager (RMI) with a high resolution of 40 microradians and a field of view of 20 milliradians, which contextualizes the LIBS chemical analyses (Le Mouélic et al., 2015). To generate the LIBS signal a pulsed laser ablates a small amount of geological samples at a microbeam scale (350-550µm diameter; (Maurice et al., 2012)) at a distance ranging between 1.56 and 7 m mostly being < 3 m. The plasma light is received by a telescope located in the mast of the rover, is separated by a de-multiplexer and transmitted to three spectrometers covering a range of 240 to 850 nm within the body of the rover (Maurice et al., 2012, 2016, Wiens et al., 2012, 2015). The emitted photon energies are analyzed by spectroscopy to determine the elemental composition of the target. Thirty laser pulses (or "shots") are usually focused on a single point, and each shot ablates some material with a depth of few µm, varying according to the target mineralogical and physical properties (Cousin et al., 2011). Compositional depth profiles can be performed for given LIBS points. For each target analyzed by ChemCam, several laser points are usually

acquired, in a raster pattern (typically rasters of 1x5, 1x10 and 3x3 points) with a spacing on the order of a few millimeters between each points. ChemCam targets were given informal names to help activity planning and data referencing. In this study, when the name is followed by a number, it corresponds to the LIBS point in the ChemCam raster observation. For example, "Lennard #1" refers to the data obtained on the first LIBS point of the target "Lennard".

Copper is detected in LIBS spectra by the elemental lines Cu I at 324.789 nm and Cu I at 327.429 nm (Goetz et al., 2017). We quantify copper only in points where the Cu I emission line at 327.428 nm is observed, using a univariate model based on the peak area of the Cu I at 324.789 nm line. Twenty natural and synthetic standards with various amounts of Cu (from 50 ppm to 1230 ppm) have been analyzed by a ChemCam replicate at Los Alamos National Laboratory (LANL, NM, USA) and were used for calibration. The resulting model has an accuracy of 41 ppm. The detection limit is 50 ppm, and the quantification limit is 165 ppm. Details of this calibration are given in the supporting material.

4 Enrichment of copper at Kimberley

We have applied the copper quantification model to ChemCam data up to Sol 1800. A few discrete targets containing anomalous elevated Cu contents have been identified along the traverse (Goetz et al., 2017) but the highest Cu abundances have been measured both by ChemCam and APXS in the potassic-rich sedimentary unit of Kimberley (Le Deit et al., 2016). We thus focus this study on this area.

In this study, Cu concentrations measured with ChemCam are qualified as "elevated" or "high" when compared to the average abundance of the terrestrial continental crust (27 ppm (Rudnick and Gao, 2003)). Cu-rich rocks and soils identified by ChemCam are localized within the stratigraphic column of Figure 1. Their compositions are shown in Table 1. The

following subsections describe the Cu-bearing targets moving up-wards in the Kimberley stratigraphy.

4.1 Liga member

Over the 15 targets analyzed by ChemCam within the Liga member (111 ChemCam LIBS points), 9 of them contain elevated Cu concentration (24 LIBS points; Figure 2a). All targets except CC_BT_0604a, which consists of soil and pebbles, are poorly sorted coarse-grained sandstones and granular conglomerate bedrock. This member was analyzed by ChemCam in different sites.

At the northern Kimberley site (Figure 1b), Lennard, a dark porous float sandstone with millimeter-sized grains, presents one LIBS point with 320 ppm Cu. The millimeter-sized granular conglomerates, Elvire #3 and Yulleroo #9, (Figure 2b) contain 325 and 465 ppm of Cu respectively (Table 1).

At the southern Kimberley site (Figure 1b), the sub-millimeter grained-size sandstone Nullara #1-2 and 4-6 and the millimeter grained-size sandstone Harms #1-3 contain an average Cu of 335 ppm and 500 ppm, respectively. These LIBS points are located in a dark matrix. In the Liga target, which is a soft sandstone (see the LIBS spot fingerprint in Figure 2a) displaying whitish and dark millimeter to sub-millimeter-sized crystals, all points except one contain elevated Cu content, ranging from 180 ppm to 1110 ppm. This target contains the highest averaged Cu concentration analyzed in Gale crater with 670 ppm (with a standard deviation of 245 ppm). Its point # 5 has the highest Cu amount measured by ChemCam, with 1110 ppm. The whitish pebble CC_BT_0604a #6 (Figure 2a) contains 815 ppm of Cu.

Finally, in the south of Kimberley (Figure 1b), the conglomerate Kalumburo with millimeter-sized grains displays two LIBS points, #3 and #5, located on dark granules that contain 130

ppm and 180 ppm of Cu respectively (Table 1, Figure 2a). A millimeter-sized dark grain on a granular conglomerate, Moogana #9, contains 555 ppm of Cu (Figure 2a).

4.2 Square Top member

Over 6 targets analyzed by ChemCam within the Square Top member (68 LIBS points), two laminated coarse-grained sandstones in the Square Top member (Figure 1b) present two points with high Cu contents. Square_top_2 #10, which partially sampled a whitish vein (according to the RMI image) at the edge of a millimeter grain- size sandstone layer, has 700 ppm of Cu (Figure 2b). Next to this rock, Eastman #16, which sampled a dark matrix in the laminated millimeter-grained size sandstone, contains 625 ppm of Cu.

4.3 Dillinger member

Over the 17 targets analyzed by ChemCam in the Dillinger member (109 LIBS points) 7 of them display Cu-rich concentrations (32 points; Table 1). Multiple targets include or consist entirely of fracture-fills: Stephen and Stephen_DP display an average of 275 ppm, Neil presents an average of 220 ppm and Mondooma #1 has 505 ppm (Figures 3b-e). In addition to copper, these three fracture-fills are enriched in manganese and zinc, sampled by several points (Lanza et al., 2016; Lasue et al., 2016). As described in (Lanza et al., 2016), Stephen and Neil are next to each other and are the flat section “of a low-angle fracture-fill that weathers in raised relief above the main sandstone outcrop surface” (Lanza et al., 2016). Mondooma #1, which is located further on the same bedrock unit, displays similar features with mm- to cm-size polygonal traces at the surface (Figure 3e). For these three fracture targets, LIBS shots removed the dust and revealed shiny dark homogeneous-looking surfaces (Figures 3d-e).

In addition to these diagenetic features, ChemCam analyzed one point located in a sub-millimeter grained-size sandstone of the Dillinger member, Wallal #3, containing high amounts of Cu (405 ppm). Lastly, 50 cm from the fracture-fills, a millimeter-sized pebble, sampled as Blina #9, contains 905 ppm of Cu (Figures 3a-b). It is found below a flat fracture-fill, oriented at a low angle that is texturally similar to Stephen, Neil and Mondooma, suggesting that the pebble comes from local erosion (several cm above Blina in Figure 3b).

4.4 Mount Remarkable

Finally, above the Dillinger member, the Mount Remarkable member presents one Cu-rich point Mahoney #4, over a total of 20 LIBS points (3 targets). It is located in the matrix at the edge of a millimeter grain-sized sandstone with 360 ppm Cu (Figure 3a).

5 Chemical composition and mineralogy of Cu-rich ChemCam LIBS points

Major, minor and trace element compositions for all the points from sedimentary materials described in the previous subsection are reported in Table 1. In agreement with elevated K_2O contents at Kimberley, the majority of Cu-rich points (57 out of 64) are also K_2O-rich, with an average of 2.0 wt. % in comparison to the Martian crust average that is estimated at 0.45 wt. % (Le Deit et al., 2016; Taylor and McLennan, 2009). This K-enrichment has also been noticed by the APXS instrument, which also observed in the Kimberley area the highest Cu content (Berger et al., 2017). These observations from APXS and ChemCam evidence that Cu is associated with potassic materials.

On Earth, copper is found in a variety of minerals such as oxides, carbonates, sulfates, sulfides (e.g., chalcopyrite $CuFeS_2$), and eventually hydrated silicates. Note that on Earth, Cu-

sulfides are widespread in Cu ore deposits, and the largest source of Cu is found in Cu porphyry settings, which are mostly alkaline (Sillitoe, 2010). The Cu-bearing phases are generally accessory minerals and may coexist with minerals like feldspars (e.g., Revett formation in Montana, (Tourtelot and Vine, 1976)). In this last case, they are usually nm to hundreds of µm in size, making it difficult to identify them as a pure phase with a typical LIBS laser beam. Therefore, this section will instead constrain larger minerals that are likely associated with Cu-bearing phases, helping us to assess the potential origin of copper enrichment in Kimberley bedrock. Although LIBS is a technique designed for chemistry, mineralogical assessment is nevertheless possible when looking at the depth profiles (e.g., (Lanza et al., 2014; Ollila et al., 2014; Payré et al., 2017)). Each LIBS shot ablates some material, enabling the 30 to 150 LIBS shots to profile up to a few microns in depth (Cousin et al., 2011). As discussed in other ChemCam studies of trace element associations (Lanza et al., 2014; Ollila et al., 2014; Payré et al., 2017), because LIBS can drill down through the mineral and potentially through the Cu-bearing phase and the host mineral, LIBS depth profiles can constrain the potential Cu-bearing phases in the bedrock and fracture-fills by revealing correlations between major element and Cu LIBS signals. In this study, correlations are considered here when squared correlation coefficients R^2 are higher than 0.4, i.e. for $R > 0.63$, which is a commonly accepted value.

To look for trends of Cu and other chemical elements, shot-to-shot trends displaying depth profiles of Cu-rich points are studied and detailed in the following subsections. Shot-to-shot results presented in the following plots exclusively show normalized intensities instead of quantitative abundances since single shot spectra are too noisy at ppm levels.

5.1 Copper association within rocks

In the drill-sampled Windjana sandstone located in the Dillinger member, CheMin detected major amounts of K-spars identified as sanidine (25.9%), plagioclase (5.4%), augite (29.3%), pigeonite (12.3%), magnetite (16.1%), olivine (7.1%), and minor amounts of ilmenite, F-apatite, hematite, pyrrhotite, akageneite and Ca-sulfate (Morrison et al., 2018; Treiman et al., 2016). In addition to the identification of these mafic and potassic phases, the occurrence of micas such as biotites have been suggested by correlations between F, Li, K, Al, Si and Mg concentrations analyzed by the ChemCam instrument in Kimberley sandstones (Forni et al., 2015; Le Deit et al., 2016). All these minerals are potentially associated with the Cu-bearing phases detected by ChemCam.

Four Cu-rich targets located in the Liga member display points for which the potential host minerals of Cu-phases can be convincingly inferred: Liga, Kalumburo #5, CC_BT_0604a #6, and Moogana #9. The oxide sum of these Cu-rich points is lower than 100 wt. %, suggesting the occurrence of several percents of one or several missing component(s). According to Figure 4, their Cu content is positively correlated to this/these element(s) supporting the association of Cu with this/these component(s), which most likely include sulfur since its detection limit with ChemCam is wt. %, i.e., too high to be detected if associated with Cu when Cu content is up to thousand of ppm (Anderson et al., 2017; Nachon et al., 2017). This suggests the occurrence of Cu-S, potentially as chalcopyrite as observed in martian meteorites (e.g., (McSween, 1994)). As previously discussed, these Cu sulfides can be associated with minerals as dissemination grains or inclusions (such as in Sudbury polymetallic deposits and in porphyry copper deposits (Ames et al., 2006; Sillitoe, 2010)). In the following paragraphs we discuss putative mineral associations within Cu-rich ChemCam points throughout the Kimberley formation (Figure 1a).

For the Liga millimeter grain sized sandstone target located in the southern Kimberley, both ChemCam and APXS analyses agree that it has the highest measured Cu content in Gale crater (an average of 680 ± 260 ppm for ChemCam and 580 ppm for APXS). This bedrock contains elevated MgO and K_2O contents (an average of MgO = 12 wt. % and K_2O = 1.6 wt. %; Table 1) in comparison with the average crust composition (MgO = 9.1 wt. % and K_2O = 0.45 wt. % respectively; (Taylor and McLennan, 2009)). In addition, this target contains one of the highest Ge contents observed in Gale crater, with Ge ~ 250 ppm according to APXS analyzes (Berger et al., 2017). Point 1 is the location displaying the most convincing shot-to-shot variations. Considering Cu I emission lines at either 324.789 or 327.428 nm, shot-to-shot analysis reveals that the Cu signal is positively correlated with K, Al, Si and Mg intensities with reasonable confidence (Figure 5a). This suggests that Cu-sulfide is associated with Mg- K- Al- silicates, potentially as clay minerals or micas like biotite. In Liga #5, the CaF molecular signal, detected by ChemCam for F concentrations > 0.2 wt. % (Forni et al., 2015), could suggest a mica like biotite (Figure 5b). A simple stoichiometric analysis exclusively based on the chemical composition measured on this point supports the occurrence of biotites along with alkali feldspars, pyroxenes, Fe- Ti - and Fe- oxides.

Located in the South of Kimberley, the cemented millimetric pebbles Kalumburo #3 and Kalumburo #5 contain the most elevated SiO_2 and Al_2O_3 contents in comparison with other Cu-rich targets in the Liga member, and #3 has the highest K_2O concentration analyzed by ChemCam in Gale crater (11.4 wt. %). Le Deit et al. (2016) suggested that this point sampled a nearly pure K-feldspar, possibly sanidine. Although shot-to-shot analysis of points #3 and #5 (also high in K_2O, at 5.9 wt. %) do not reveal any clear correlation with Cu signal (e.g., #3 in Fig. S4), it is reasonable to suggest that Cu-S could be associated with the K-feldspar identified in Le Deit et al. (2016). These sulfides could occur as disseminated grains or

inclusions as observed in some Cu deposits on Earth, such as the ore bodies located at Mount Miligan in British Columbia (disseminated chalcopyrites within alkali feldspar; (Laznicka, 2010)).

With 820 ppm of Cu, the millimetric whitish pebble CC_BT_0604a #6 contains higher MgO and lower Na_2O than other Cu-bearing points located in the northern Kimberley (MgO = 8.6 wt. % and Na_2O = 2.0 wt. %; Table 1). Shot-to-shot analysis shows a strong increase of Cu with depth and positive correlations between Cu and Ti signals with a R^2 = 0.8 (Figure 6). Weaker positive correlations between Cu and Al and K signals are also observed (Figure 6). Therefore, despite a high MgO content, the Cu-sulfide is likely associated within a Ti- Al-bearing potassic phase, the nature of which is difficult to assess.

Finally, also in the South of Kimberley, the millimeter grain size conglomerate Moogana #9 has higher MgO and FeO contents than Kalumburo #3 and 5 and lower K_2O content, which yet remains elevated in comparison with the averaged martian bulk crust (Table 1). In addition, shot-to-shot analysis reveals that Ca, Si, Mg, and Fe signals are positively correlated with Cu, while Ti intensities are inversely correlated with Cu (Figure 7). This indicates that Moogana would preferentially bear Cu-S mixed with a Ca- Mg- Fe- bearing silicate such as pigeonite pyroxene, which is consistent with stoichiometric analysis indicating Fe-Mg-pyroxenes coexisting with alkali feldspars and Fe-oxides.

To summarize, in the Kimberley bedrock, copper is likely found as chalcopyrite preferentially occurring in potassic-rich materials (K_2O ranging between 0.9 and 11.4 wt. % in comparison with the averaged martian crustal content of 0.45 wt. %, Taylor and McLennan, 2009). Most Cu-rich points contain low SiO_2 (an average of 45.1 wt. %), and high MgO or FeO contents

(up to 16.2 wt. % and 42.9 wt. % respectively). No pure Cu-sulfide the size of the laser beam was analyzed by ChemCam, as the Cu content would have been far higher along with visible S signals in LIBS spectra. The Cu-sulfide grains are thus smaller than the laser beam diameter (~350 µm). They are likely associated with potassic silicates like K-feldspars, K-micas or K-clay minerals, as well as with mafic minerals like pyroxenes, which have all been detected by CheMin within the Windjana sample except for K-micas which are consistent with the Windjana composition analyzed by ChemCam, specifically indicated by the presence of fluorine. These sparse Cu-sulfides were not detected by CheMin within the Windjana sample, which is not surprising since no Cu was observed by ChemCam in all the Windjana targets (sols 612, 619, 622, and 625).

5.2 Copper within fracture-fills

In the Dillinger member, all fracture-fills displaying high amounts of manganese contain elevated copper contents, between 150 and 530 ppm (Lanza et al., 2016). They contain elevated magnesium contents in comparison with the Martian crust (MgO = 9.6 - 16.2 wt. %), and their potassium abundance is the lowest analyzed at Kimberley, with an average K_2O of 1.7 wt. %. Some ChemCam points in Neil and Mondooma also display high zinc contents (Zn > 5000 ppm) in comparison with the average crust (320 ppm; (Lasue et al., 2016; Taylor and McLennan, 2009)).

According to Figure 8, in fracture-fills, manganese abundances increase with copper content. Cu is thus likely associated with Mn phases. As demonstrated in Lanza et al. (2016), these Mn phases are likely Mn oxides. Moreover, in Stephen, APXS measured high Cl, Ni, Co, Zn and Mn contents, and Cu, Mn and Ni are correlated (Lanza et al., 2016). Several metals like Cu, Ni and Zn are well known to be adsorbed on the surface of these oxides in terrestrial settings (e.g., (Murray, 1975)).

In most ChemCam observation points of these fracture-fills, Mn and Cu signals decrease with depth. The clearest evidence of this is found in Stephen target. Indeed, three points were analyzed by 150 LIBS shots in an observation sequence called Stephen_DP (DP = depth profile) in order to provide accurate depth-profile LIBS analyses. The decrease of Cu and Mn emission lines with depth is clearly observed (Figure 9a). Figure 9b shows that Cu and Mn signals strongly decrease until shot 70, and then remain quite constant. In contrast, Si, Al, Ca, K, Fe and Mg mostly increase until around shot 30 and are well correlated to each other, suggesting the occurrence of Al-Ca-K-Fe-Mg-bearing silicates like a mixing of pyroxene and feldspar. Overall, these observations support the existence of a compositionally stratified fracture-fill, in agreement with the MAHLI images presented in Figure 2d of Lanza et al. (2016), showing light material within LIBS ablation pits in comparison with the dark surface which has low reflectance, characteristic of Mn-oxides (Fox et al., 2015; Hardgrove et al., 2015; Lanza et al., 2016). As a result, Cu adsorption on Mn oxides is likely occurring at the surface, with a transition to Al-Ca-K-Fe-Mg-bearing silicates at depth, potentially as pyroxenes and/or feldspars.

In addition, in Neil #8 displaying ZnO = 0.7 wt. %, shot-to-shot analysis reveal positive correlations between Cu signals and Mn, and weak positive correlations between Cu and Na and Zn intensities (Figure 9c). These observations can be explained by adsorptions of Cu and Zn on sodic-manganese oxides, potentially indicating sodic birnessite, as typically observed on Earth (Della Puppa et al., 2013).

In summary, these fracture-fill compositions all change with depth, the surface being enriched in manganese oxides that have adsorbed copper (and zinc), and the deeper phases likely being minerals phases such as alkali feldspars and pyroxenes, as observed by CheMin in the Windjana drill sample (Treiman et al., 2016).

6 Provenance of copper in Gale crater

6.1 Scenario of Cu enrichments at Kimberley

Copper mineralogical associations are distinct between bedrock and fractures: Cu-sulfides are likely associated with silicates in potassic bedrock settings while Cu is likely adsorbed on manganese oxides in fracture-fill materials. Elevated copper concentrations would thus be related to two distinct processes. Although more complex scenarios are possible, we propose the following phases of copper enrichments at Kimberley:

(1) In sedimentary bedrock, the occurrence of Cu-sulfides in localized points in potassic sandstones and conglomerates at Kimberley suggests that they are detrital, similarly to most mafic and K-silicates of the Kimberley formation (Forni et al., 2015; Le Deit et al., 2016; Treiman et al., 2016). Cu-sulfides may have thus been associated with feldspars and pyroxenes when these latter formed. Since these silicates are thought to come from K-rich igneous rocks and/or low-alkali basaltic rocks located in the crater's northwestern rim or the catchment basin upstream of the rim (Le Deit et al., 2016; Treiman et al., 2016), Cu-sulfides could have originated from the same sources, and would have been transported along with potassic minerals down the fluvial channel to Kimberley where they were deposited, forming the observed sedimentary bedrock.

(2) The fracturing of this sedimentary bedrock and the circulation of a Mn-rich groundwater would have led to the precipitation of manganese oxides in oxidizing conditions at circumneutral pH (Lanza et al., 2016). Subsequently, cation metals Cu^{2+} and Zn^{2+} would have been adsorbed on their surface.

Having determined a plausible scenario explaining how copper arrived in Kimberley bedrock and fracture-fills, it is of interest to constrain its initial provenance, as discussed in the following subsections.

6.2 Provenance of copper concentrated within the Kimberley sedimentary rocks

Focusing on the Kimberley sedimentary rocks, the Cu-rich points mainly contain relatively elevated magnesium and potassium concentrations with an average MgO abundance of 10.5 wt. %, and K_2O = 2.0 wt. % (Table 1). These grains are mostly detrital, coming from potassic and/or mafic igneous source(s) (Treiman et al., 2016).

In addition to the sedimentary bedrock, ChemCam measured elevated copper concentrations in several points of igneous rocks dated from Noachian (> 3.8 Gyr; (Cousin et al., 2017; Sautter et al., 2015)). These include a weathered leucocratic quartzodiorite/ granodiorite float called Angmaat (Sol 337) analyzed before reaching the Kimberley area, and a porphyric trachyandesite float named Angelo (Sol 553) encountered at the base of the Kimberley formation at Point Coulomb. Both of these igneous rocks contain high Cu within the matrix and individual feldspars up to 1000 ppm in point #8 of the Angelo target (Figures 10a-b; composition is shown in Table 1) (Cousin et al., 2017). This high copper location corresponds to an andesine composition and displays a high H signal (Figure 10c). This composition falls into the immiscibility zone most likely due to mixing between distinct feldspar compositions. This could be due to the development of exsolution lamellae as the primary igneous material cooled or could be the result of compositional mixing within the LIBS plasma, which occurs if the target grain sizes are significantly smaller than the laser spot size (< 1.0 mm). Copper was likely associated with this feldspar during crystallization, which is suggestive of either mid to late stage differentiation in a magmatic system or a low degree of partial melting based on the trachytic nature of Angelo and the occurrence of andesine minerals (Sautter et al., 2016).

Such elevated Cu concentrations in sedimentary and igneous rocks (up to 1100 ppm) suggest an ore deposit at the source. The Cu-sulfides are spread and unequally distributed in rocks

within the Kimberley formation, suggesting that they were disseminated at the source as commonly observed in terrestrial ore deposits (Ridley, 2013). In the following subsections, although other scenarios are possible, we discuss three potential provenances of copper.

6.2.1 Is copper coming from a Martian porphyry copper deposit?

On Earth, porphyry copper deposits are magmatic bodies that cooled rapidly, creating porphyritic igneous rocks ((Richards, 2016); and citations therein). The igneous rocks usually associated with this kind of deposit are mainly alkaline rocks ((Berger et al., 2008); and references therein). The currently accepted formation model is that hydrothermal fluids coming from the magma partition metals like copper and gold, and are mixed with S-rich magmatic gases, precipitating sulfides including those bearing Cu. Thus, in these deposits, Cu is mainly associated with sulfide mineral veins and/or disseminated grains ((Lowell and Guilbert, 1970; Richards, 2016); and references therein). All around the magma body, a zoning pattern occurs, including a potassic alteration zone forming K- and Mg- rich minerals such as K-spars, biotites, and commonly including apatites. These deposits are typically related to magmas generated during or after subduction mainly due to two fundamental melting parameters: relatively high oxidation state above the fayalite-magnetite-quartz buffer (QFM, typically QFM +2) enhancing melts with chalcophile metals, and high water contents saturating the magma in an aqueous phase where metals effectively partition (e.g., H_2O > 4.0 %; (Richards, 2009; Sillitoe, 2010)). On Mars, these two critical characteristics are thought to have been produced in ancient melts without the necessity of subduction settings. For example, there is significant evidence for high oxidation states up to 3 log units above QFM in the uppermost mantle (Herd, 2003; Tuff et al., 2013), and evidence for S-rich hydrated magmas potentially containing more than 1% of H_2O and S in Noachian time (Gaillard and Scaillet, 2009; Herd, 2003; McCubbin et al., 2012; McSween et al., 2001)).

The occurrence of elevated Cu concentrations in potassic sandstones and in felsic and alkaline igneous rocks at Kimberley can thus suggest the occurrence of a porphyry copper deposit at the source region of the Kimberley bedrock. The elevated Zn and Ge concentrations measured by APXS in potassic sandstones (Zn up to 4000 ppm) and in the Liga target (Ge = 250 ppm) respectively, suggests high temperature hydrothermal activity localized in the source region of these materials (Berger et al., 2017; Thompson et al., 2016). This would favor the formation of an ore body around the magma intrusion, from which the potassic minerals encountered at Kimberley may have originated.

If the Cu found at Kimberley came from a porphyry deposit, we can envision that an alkaline magma would have cooled rapidly, forming a potassic alteration zone around this magmatic body. Hydrothermal circulation would have concentrated copper within sulfide minerals and/or the remaining melt. Erosion, alteration and transportation of the resulting igneous rocks, Cu-sulfides, and K-Mg-rich minerals from the potassic alteration zones to Kimberley would explain both the elevated metal concentrations within sedimentary rocks, and the origin of the K-Mg-rich minerals.

6.2.2 Is impact-induced hydrothermal alteration the origin of copper enrichments?

An alternative scenario would be the association of Cu sulfides with silicates by alteration at high temperature. Impact-induced hydrothermal alteration could be a reasonable possibility: the high temperature induced by an impact can melt and heat a large volume of rocks, providing an efficient source for hydrothermal activity. Indeed, interactions between these heated rocks with near-surface H_2O leads to hot water circulations that enhance water-rock interactions (e.g., (Osinski et al., 2005)). This phenomenon, which has been widely suggested on Mars (e.g., (Allen et al., 1982; Newsom et al., 1996; Schwenzer et al., 2012; Schwenzer and Kring, 2009)), can thus result in the formation of ore deposits by remobilization of metals

and re-deposition within fractures and breccias, as observed on Earth in Sudbury and Haughton craters (Ames et al., 1998; Osinski et al., 2001).

The occurrence of elevated amounts of copper within the trachyandesite Angelo suggests that Cu may have been incorporated in igneous matrix and plagioclase during magma melting. Since Cu behaves as a compatible element during magmatic crystallization, this porphyric igneous rock could be the evidence of a supply of copper within the melt, certainly from a mafic magma. Hydrothermal fluids generated by the impact would have re-mobilized this element and potentially other metals not detected by ChemCam, weathered these felsic igneous rocks located on the crater floor, and re-deposited copper in association with resulting igneous feldspar, pyroxene and other silicates. Finally, these minerals would have been transported by the fluvial system to Kimberley where they were deposited. Other metals including noble metals commonly found in association with these Cu-deposits on Earth may also occur in Gale crater (e.g., (Ames et al., 1998; Osinski et al., 2001)).

In Sudbury and Haughton craters, the deposition of sulfide minerals including chalcopyrite likely occurred at temperatures between 100 °C and 200 °C (Ames et al., 2006; Osinski et al., 2005), which means that on Mars, a hydrothermal system at an impact crater with a diameter varying from 30 to 200 km can provide fluids heated sufficiently to form these minerals (although the lifetime of the hydrothermal system would be shorter in small impact crater) (Abramov and Kring, 2005).

6.2.3 Are copper enrichments related to fumarolic activities?

On Earth, fumaroles emit steam and gases like CO_2, H_2O and H_2S that escape and often sublimate metals located in volcanic ash layers at the surface (e.g., (Henley and Berger, 2012)). Depending on the physical and chemical gas conditions, the vapor phase of fumaroles

can concentrate enough metals to permit the formation of ore deposits including Cu-deposits (Henley and Berger, 2012; Williams-Jones and Heinrich, 2005).

The Kimberley sedimentary rocks may share the same sources as several consolidated, thinly laminated, fine-grained float rocks located in and near the Bathurst Inlet outcrop at Yellowknife Bay since they display similar K_2O and MgO compositions (Le Deit et al., 2016; Thompson et al., 2016). The nature of these latter rocks remains uncertain, whether volcaniclastic or sedimentary sandstones (Mangold et al., 2015; Sautter et al., 2013), but according to several studies, the occurrence of small volumes of K-rich rocks restricted to certain beds in Yellowknife Bay strengthens the idea of volcanic ash introduction in Gale crater basin, forming later volcaniclastic layers (McLennan et al., 2014; Sautter et al., 2013; Schmidt et al., 2013). Interestingly, float rocks of similar morphology and nearly identical composition were found in the Bimbe heterolithic unit some 9 km away from the Bathurst-type layered rocks (Wiens et al., 2017), suggesting the widespread deposition of Mg- and K-rich float rocks. If these kind of potassic volcaniclastic rocks indeed occur in Gale crater, a potassic explosive volcanism would have been necessary to create these immature K-rich ash beds potentially formed by feldspars and other K-silicates, as observed on Earth in the tuffs of the Yucca Mountain (Sheridan, 1970). Fumarolic activities among earlier K-rich sedimentary beds could have concentrated metals including Cu as sulfides upstream of Gale crater within the potassic ash beds in association with feldspars and other silicates as observed in the phreatic ash layers of Mount St Helens, deposited in 1980 (Thomas et al., 1982).

6.3 Origin of Cu enrichments in fractures, and environmental implications

As discussed in Section 6.1, nickel, copper and zinc in fracture-fills were likely adsorbed on manganese oxides (Lanza et al., 2016). A potential origin of these cation metals is from weathering of the local bedrock. However, the low alteration and the occurrence of elevated

contents of Zn and Ni, especially in fracture-fills, suggest an external origin rather than in situ rock weathering (Berger et al., 2017; Lasue et al., 2016). On Earth, these elements are typically initially hosted in mafic rocks, and have a great affinity for Fe-bearing minerals in igneous and sedimentary rocks (De Vos et al., 2005; Sluzhenikin et al., 2014). Therefore, they could come from a mafic source similar to basalts and gabbros encountered along the traverse, or from a Fe-mineral-bearing sedimentary source like magnetite or hematite, as detected by CheMin in the Rocknest sand and the Murray sedimentary materials (Blake et al., 2013; Hurowitz et al., 2017).

Manganese oxides are scavengers of trace metals like Cu^{2+}, Ni^{2+} and Zn^{2+} in marine and fresh water (Murray, 1975). Studies of natural and synthetic manganese oxides like birnessite, vernadite and hydrous MnO_2 show an increase of divalent metallic cation sorption, especially with increasing pH; the circulation of a hot fluid is not needed for this kind of mechanism (e.g., sorption in fresh- or sea- water (Manceau et al., 2007; Murray, 1975)). As shown in the stability diagram on Figure 11, Mn^{2+} is soluble over a large range of redox conditions in acidic environments, and precipitates as Mn-oxides in highly oxidizing environments (Eh > +500 mV). Cu^{2+}, Ni^{2+} and Zn^{2+} are mobile in acidic and oxidizing conditions (Guilbert and Park, 2007), and the fraction of Cu, Ni and Zn sorbed on MnO_2 increases with pH, even in alkali environments (Murray, 1975). In the Dillinger member, if the precipitation of manganese oxides and the enrichments of zinc, nickel and copper occurred during the same episode, as is likely, the metal-bearing fluid would thus have been highly oxidizing (Eh > +500 mV) at circum-neutral pH (~ 7) in order to enhance the adsorption of metals (Lanza et al., 2016). If these precipitations and adsorptions are distinct events, the pH and redox ranges of the fluids would be larger: a strongly oxidizing fluid would precipitate MnO_2 at a circum-neutral pH as described by (Lanza et al., 2016), and later, Cu^{2+} and Zn^{2+} would be adsorbed in oxidizing circum-neutral conditions (Eh > +200 mV, pH ~ 7). In both cases, the precipitation

of manganese oxides and the adsorption of metals is characteristic of the circulation of an oxidizing fluid, certainly at low temperature.

7 Conclusion

For the first time, copper abundances are quantified using LIBS in materials analyzed by ChemCam, with an accuracy of 41 ppm. The most elevated copper concentrations along the Curiosity traverse in Gale crater are observed at Kimberley in two kinds of sedimentary materials: within potassic bedrock containing high magnesium contents, and within manganese-rich fracture-fills.

In bedrock, Cu-minerals are likely sulfides such as chalcopyrite, and are mainly associated with detrital silicates including K-feldspars, K-phyllosicates, and pyroxenes. In the diagenetic features, copper and in a number of cases also zinc are found in association with manganese oxides that appear to have precipitated from highly oxidizing circum-neutral groundwater (Lanza et al., 2016). These two distinct mineralogical associations suggest at least two petrogenetic processes and distinct sources:

(1) Cu-sulfides in bedrock likely share the same sources as their detrital potassic and mafic mineral hosts: they would come from K-rich and/or mafic igneous rocks located in the northern rim of the crater or in the catchment basin beyond the rim (Le Deit et al., 2016; Treiman et al., 2016). Such elevated copper amounts suggest the occurrence of a copper deposit related to hydrothermal circulation. This could be a porphyry copper deposit, a region of impact-induced hydrothermal activity, or a region of fumarolic activity sourced in volcanoclastic rocks. After the erosion and alteration of this deposit, Cu-sulfides and potassic and mafic minerals would have been transported by the fluvial system and deposited at Kimberley, forming sedimentary bedrock.

(2) After the fracturing of the sedimentary bedrock, a Mn-rich oxidizing fluid would have precipitated Mn oxides within the fractures, and Cu and other metals including Zn and Ni would have been adsorbed at their surface. These compatible metallic cations are potentially coming from mafic igneous rocks like basalts, or Fe-bearing materials like magnetite as commonly observed on Earth (De Vos et al., 2005; Sluzhenikin et al., 2014). A fluid, likely at low temperature, would have leached the host rocks, and an oxidizing solution would have led to the adsorption of these metals on the manganese oxides surface.

Relatively high copper concentrations studied in a single region of Gale crater highlight again the complexity of the past Martian magmatism and weathering, and suggest the presence of a copper deposit in the northern Gale crater rim or the catchment basin beyond the rim. The discovery of evolved igneous rocks in Gale crater provides new insights about the potential occurrence of metal deposits on Mars.

Acknowledgements

All the major element and copper contents of standards and ChemCam points discussed here are listed in the supplementary table and can be found in http://pds-geosciences.wustl.edu/missions/msl/chemcam.htm. The MSL teams are thanked for their part in this work.

Funding : This work was carried out with funding from CNRS and CNES in France and by NASA's Mars Exploration Program in the US.

8 References

Abramov, O., Kring, D.A., 2005. Impact-induced hydrothermal activity on early Mars. J. Geophys. Res. Planets 110. https://doi.org/10.1029/2005JE002453

Allen, C.C., Gooding, J.L., Keil, K., 1982. Hydrothermally altered impact melt rock and breccia: Contributions to the soil of Mars. J. Geophys. Res. Solid Earth 87, 10083–10101. https://doi.org/10.1029/JB087iB12p10083

Ames, D.E., Jonasson, I.R., Gibson, H.L., Pope, K.O., 2006. Impact-Generated Hydrothermal System ? Constraints from the Large Paleoproterozoic Sudbury Crater, Canada, in: Cockell, C., Gilmour, I., Koeberl, C. (Eds.), Biological Processes Associated with Impact Events. Springer-Verlag, Berlin/Heidelberg, pp. 55–100. https://doi.org/10.1007/3-540-25736-5_4

Ames, D.E., Watkinson, D.H., Parrish, R.R., 1998. Dating of a regional hydrothermal system induced by the 1850 Ma Sudbury impact event. Geology 26, 447. https://doi.org/10.1130/0091-7613(1998)026<0447:DOARHS>2.3.CO;2

Anderson, D.E., Ehlmann, B.L., Forni, O., Clegg, S.M., Cousin, A., Thomas, N.H., Lasue, J., Delapp, D.M., McInroy, R.E., Gasnault, O., Dyar, M.D., Schröder, S., Maurice, S., Wiens, R.C., 2017. Characterization of LIBS emission lines for the identification of chlorides, carbonates, and sulfates in salt/basalt mixtures for the application to MSL ChemCam data. J. Geophys. Res. Planets 122, 744–770. https://doi.org/10.1002/2016JE005164

Arvidson, R.E., Squyres, S.W., Bell, J.F., Catalano, J.G., Clark, B.C., Crumpler, L.S., Souza, P.A. de, Fairén, A.G., Farrand, W.H., Fox, V.K., Gellert, R., Ghosh, A., Golombek, M.P., Grotzinger, J.P., Guinness, E.A., Herkenhoff, K.E., Jolliff, B.L., Knoll, A.H., Li, R., McLennan, S.M., Ming, D.W., Mittlefehldt, D.W., Moore, J.M., Morris, R.V., Murchie, S.L., Parker, T.J., Paulsen, G., Rice, J.W., Ruff, S.W., Smith, M.D., Wolff, M.J., 2014. Ancient Aqueous Environments at Endeavour Crater, Mars. Science 343, 1248097. https://doi.org/10.1126/science.1248097

Baknes, M.E., 1990. A Structural-Geochemical Investigation of a Mineralized Breccia and Associated Vein System at the Contact of the Strathy Batholith and the Temagami Greenstone Belt, Strathy TWP., Ontario. (Thesis).

Banham, S.G., Gupta, S., Rubin, D.M., Watkins, J.A., Sumner, D.Y., Edgett, K.S., Grotzinger, J.P., Lewis, K.W., Edgar, L.A., Stack- Morgan, K.M., Barnes, R., Bell, J.F., Day, M.D., Ewing, R.C., Lapotre, M.G.A., Stein, N.T., Rivera- Hernandez, F., Vasavada, A.R., 2018. Ancient Martian aeolian processes and palaeomorphology reconstructed from the Stimson formation on the lower slope of Aeolis Mons, Gale crater, Mars. Sedimentology 65, 993–1042. https://doi.org/10.1111/sed.12469

Berger, B.R., Ayuso, R.A., Wynn, J.C., R, R., Seal, I.I., 2008. Preliminary Model of Porphyry Copper Deposits (No. 2008–1321). Geological Survey (U.S.).

Berger, J.A., Schmidt, M.E., Gellert, R., Boyd, N.I., Desouza, E.D., Flemming, R.L., Izawa, M.R.M., Ming, D.W., Perrett, G.M., Rampe, E.B., Thompson, L.M., VanBommel, S.J.V., Yen, A.S., 2017. Zinc and Germanium in the Sedimentary Rocks of Gale Crater on Mars Indicate Hydrothermal Enrichment Followed by Diagenetic Fractionation. J. Geophys. Res. Planets. https://doi.org/10.1002/2017JE005290

Blake, D.F., Morris, R.V., Kocurek, G., Morrison, S.M., Downs, R.T., Bish, D., Ming, D.W., Edgett, K.S., Rubin, D., Goetz, W., Madsen, M.B., Sullivan, R., Gellert, R., Campbell, I., Treiman, A.H., McLennan, S.M., Yen, A.S., Grotzinger, J., Vaniman, D.T., Chipera, S.J., Achilles, C.N., Rampe, E.B., Sumner, D., Meslin, P.-Y., Maurice, S., Forni, O., Gasnault, O., Fisk, M., Schmidt, M., Mahaffy, P., Leshin, L.A., Glavin, D., Steele, A., Freissinet, C., Navarro-Gonzalez, R., Yingst, R.A., Kah, L.C., Bridges, N., Lewis, K.W., Bristow, T.F., Farmer, J.D., Crisp, J.A., Stolper, E.M., Des Marais, D.J., Sarrazin, P., MSL Science Team, Agard, C., Alves Verdasca, J.A., Anderson, R., Anderson, R., Archer, D., Armiens-Aparicio, C., Arvidson, R., Atlaskin, E., Atreya, S., Aubrey, A., Baker, B., Baker, M., Balic-Zunic, T., Baratoux, D., Baroukh, J., Barraclough, B., Bean, K., Beegle, L., Behar, A., Bell, J., Bender, S., Benna, M., Bentz, J., Berger, G., Berger, J., Berman, D., Blanco Avalos, J.J., Blaney, D., Blank, J., Blau, H., Bleacher, L., Boehm, E., Botta, O., Bottcher, S., Boucher, T., Bower, H.,

Boyd, N., Boynton, B., Breves, E., Bridges, J., Brinckerhoff, W., Brinza, D., Brunet, C., Brunner, A., Brunner, W., Buch, A., Bullock, M., Burmeister, S., Cabane, M., Calef, F., Cameron, J., Cantor, B., Caplinger, M., Rodriguez, J.C., Carmosino, M., Blazquez, I.C., Charpentier, A., Choi, D., Clark, B., Clegg, S., Cleghorn, T., Cloutis, E., Cody, G., Coll, P., Conrad, P., Coscia, D., Cousin, A., Cremers, D., Cros, A., Cucinotta, F., d'Uston, C., Davis, S., Day, M., Juarez, M. d. l. T., DeFlores, L., DeLapp, D., DeMarines, J., Dietrich, W., Dingler, R., Donny, C., Drake, D., Dromart, G., Dupont, A., Duston, B., Dworkin, J., Dyar, M.D., Edgar, L., Edwards, C., Edwards, L., Ehlmann, B., Ehresmann, B., Eigenbrode, J., Elliott, B., Elliott, H., Ewing, R., Fabre, C., Fairen, A., Farley, K., Fassett, C., Favot, L., Fay, D., Fedosov, F., Feldman, J., Feldman, S., Fitzgibbon, M., Flesch, G., Floyd, M., Fluckiger, L., Fraeman, A., Francis, R., Francois, P., Franz, H., French, K.L., Frydenvang, J., Gaboriaud, A., Gailhanou, M., Garvin, J., Geffroy, C., Genzer, M., Godber, A., Goesmann, F., Golovin, D., Gomez, F.G., Gomez-Elvira, J., Gondet, B., Gordon, S., Gorevan, S., Grant, J., Griffes, J., Grinspoon, D., Guillemot, P., Guo, J., Gupta, S., Guzewich, S., Haberle, R., Halleaux, D., Hallet, B., Hamilton, V., Hardgrove, C., Harker, D., Harpold, D., Harri, A.-M., Harshman, K., Hassler, D., Haukka, H., Hayes, A., Herkenhoff, K., Herrera, P., Hettrich, S., Heydari, E., Hipkin, V., Hoehler, T., Hollingsworth, J., Hudgins, J., Huntress, W., Hurowitz, J., Hviid, S., Iagnemma, K., Indyk, S., Israel, G., Jackson, R., Jacob, S., Jakosky, B., Jensen, E., Jensen, J.K., Johnson, J., Johnson, M., Johnstone, S., Jones, A., Jones, J., Joseph, J., Jun, I., Kahanpaa, H., Kahre, M., Karpushkina, N., Kasprzak, W., Kauhanen, J., Keely, L., Kemppinen, O., Keymeulen, D., Kim, M.-H., Kinch, K., King, P., Kirkland, L., Koefoed, A., Kohler, J., Kortmann, O., Kozyrev, A., Krezoski, J., Krysak, D., Kuzmin, R., Lacour, J.L., Lafaille, V., Langevin, Y., Lanza, N., Lasue, J., Le Mouelic, S., Lee, E.M., Lee, Q.-M., Lees, D., Lefavor, M., Lemmon, M., Lepinette Malvitte, A., Leveille, R., Lewin-Carpintier, E., Li, S., Lipkaman, L., Little, C., Litvak, M., Lorigny, E., Lugmair, G., Lundberg, A., Lyness, E.,

Maki, J., Malakhov, A., Malespin, C., Malin, M., Mangold, N., Manning, H., Marchand, G., Marin Jimenez, M., Martin Garcia, C., Martin, D., Martin, M., Martinez-Frias, J., Martin-Soler, J., Martin-Torres, F.J., Mauchien, P., McAdam, A., McCartney, E., McConnochie, T., McCullough, E., McEwan, I., McKay, C., McNair, S., Melikechi, N., Meyer, M., Mezzacappa, A., Miller, H., Miller, K., Milliken, R., Minitti, M., Mischna, M., Mitrofanov, I., Moersch, J., Mokrousov, M., Molina Jurado, A., Moores, J., Mora-Sotomayor, L., Morookian, J.M., Mueller-Mellin, R., Muller, J.-P., Munoz Caro, G., Nachon, M., Navarro Lopez, S., Nealson, K., Nefian, A., Nelson, T., Newcombe, M., Newman, C., Newsom, H., Nikiforov, S., Niles, P., Nixon, B., Dobrea, E.N., Nolan, T., Oehler, D., Ollila, A., Olson, T., Owen, T., Pablo, H., Paillet, A., Pallier, E., Palucis, M., Parker, T., Parot, Y., Patel, K., Paton, M., Paulsen, G., Pavlov, A., Pavri, B., Peinado-Gonzalez, V., Pepin, R., Peret, L., Perez, R., Perrett, G., Peterson, J., Pilorget, C., Pinet, P., Pla-Garcia, J., Plante, I., Poitrasson, F., Polkko, J., Popa, R., Posiolova, L., Pradler, I., Prats, B., Prokhorov, V., Purdy, S.W., Raaen, E., Radziemski, L., Rafkin, S., Ramos, M., Raulin, F., Ravine, M., Reitz, G., Renno, N., Rice, M., Richardson, M., Robert, F., Rodriguez Manfredi, J.A., Romeral-Planello, J.J., Rowland, S., Saccoccio, M., Salamon, A., Sandoval, J., Sanin, A., Sans Fuentes, S.A., Saper, L., Sautter, V., Savijarvi, H., Schieber, J., Schmidt, W., Scholes, D., Schoppers, M., Schroder, S., Sebastian Martinez, E., Sengstacken, A., Shterts, R., Siebach, K., Siili, T., Simmonds, J., Sirven, J.-B., Slavney, S., Sletten, R., Smith, M., Sobron Sanchez, P., Spanovich, N., Spray, J., Squyres, S., Stack, K., Stalport, F., Stein, T., Stern, J., Stewart, N., Stipp, S.L.S., Stoiber, K., Sucharski, B., Summons, R., Sun, V., Supulver, K., Sutter, B., Szopa, C., Tate, C., Teinturier, S., ten Kate, I.L., Thomas, P., Thompson, L., Tokar, R., Toplis, M., Torres Redondo, J., Trainer, M., Tretyakov, V., Urqui-O'Callaghan, R., Van Beek, J., Van Beek, T., VanBommel, S., Varenikov, A., Vasavada, A., Vasconcelos, P., Vicenzi, E., Vostrukhin, A., Voytek, M., Wadhwa, M., Ward, J., Webster, C., Weigle, E., Wellington, D., Westall, F.,

Wiens, R.C., Wilhelm, M.B., Williams, A., Williams, J., Williams, R., Williams, R.B., Wilson, M., Wimmer-Schweingruber, R., Wolff, M., Wong, M., Wray, J., Wu, M., Yana, C., Zeitlin, C., Zimdar, R., Zorzano Mier, M.-P., 2013. Curiosity at Gale Crater, Mars: Characterization and Analysis of the Rocknest Sand Shadow. Science 341, 1239505–1239505. https://doi.org/10.1126/science.1239505

Boctor, N.Z., Meyer, H.O.A., Kullerud, G., 1976. Lafayette meteorite: petrology and opaque mineralogy. Earth Planet. Sci. Lett. 32, 69–76. https://doi.org/10.1016/0012-821X(76)90186-2

Bunch, T.E., Reid, A.M., 1975. The nakhlites part I: petrography and mineral chemistry. Meteoritics 10, 303–315. https://doi.org/10.1111/j.1945-5100.1975.tb01187.x

Cousin, A., Maurice, S., Berger, G., Forni, O., Gasnault, O., Wiens, R.C., the ChemCam team, 2011. Depth Profiles Studies using ChemCam, in: Lunar and Planetary Science Conference. Presented at the Lunar and Planetary Science Conference.

Cousin, A., Sautter, V., Payré, V., Forni, O., Mangold, N., Gasnault, O., Le Deit, L., Johnson, J., Maurice, S., Salvatore, M., Wiens, R.C., Gasda, P., Rapin, W., 2017. Classification of igneous rocks analyzed by ChemCam at Gale crater, Mars. Icarus 288, 265–283. https://doi.org/10.1016/j.icarus.2017.01.014

De Vos, W., Batista, M.J., Demetriades, A., Duris, M., Lexa, J., Lis, J., Marsina, K., O'Connor, P.J., 2005. Metallogenic mineral provinces and world class ore deposits in Europe. Geochem. Atlas … Part, 1, 43–49.

Della Puppa, L., Komárek, M., Bordas, F., Bollinger, J.-C., Joussein, E., 2013. Adsorption of copper, cadmium, lead and zinc onto a synthetic manganese oxide. J. Colloid Interface Sci. 399, 99–106. https://doi.org/10.1016/j.jcis.2013.02.029

Forni, O., Gaft, M., Toplis, M.J., Clegg, S.M., Maurice, S., Wiens, R.C., Mangold, N., Gasnault, O., Sautter, V., Le Mouélic, S., Meslin, P.-Y., Nachon, M., McInroy, R.E., Ollila,

A.M., Cousin, A., Bridges, J.C., Lanza, N.L., Dyar, M.D., 2015. First detection of fluorine on Mars: Implications for Gale Crater's geochemistry: First detection of fluorine on Mars. Geophys. Res. Lett. 42, 1020–1028. https://doi.org/10.1002/2014GL062742

Forni, O., Vaniman, D.T., Le Deit, L., Clegg, S.M., Lanza, N.L., Lasue, J., Bish, D.L., Mangold, N., Wiens, R.C., Meslin, P.-Y., Gasnault, O., Maurice, S., Cousin, A., Toplis, M.J., Newsom, H., Rampe, E.B., 2015. Fluorine and Lithium at the Kimberley Outcrop, Gale Crater, in: 46th Lunar and Planetary Science Conference. Lunar and Planetary Institute, Houston, p. Abstract #1989.

Fox, V.K., Arvidson, R.E., Jolliff, B.L., Carpenter, P.K., Catalano, J.G., Hinkle, M.A.G., Morris, R.V., 2015. Characterization of Synthetic and Natural Manganese Oxides as Martian Analogues. Presented at the Lunar and Planetary Science Conference, p. 2132.

Gaillard, F., Scaillet, B., 2009. The sulfur content of volcanic gases on Mars. Earth Planet. Sci. Lett. 279, 34–43. https://doi.org/10.1016/j.epsl.2008.12.028

Gellert, R., Boyd, N., Campbell, J.L., VanBommel, S., Thompson, L.M., Schmidt, M.E., Berger, J.A., Clark, B.C., Grotzinger, J.P., Yen, A.S., Fisk, M.R., 2014. Apxs Chemical Composition of the Kimberley Sandstone in Gale Crater. AGU Fall Meet. Abstr.

Goetz, W., Payré, V., Wiens, R.C., Gasnault, O., Gellert, R., Newsom, H., Fabre, C., Forni, O., Lasue, J., Meslin, P.-Y., Maurice, S., Frydenvang, J., Clark, B., Team, M.S., 2017. Detection of Copper by the ChemCam Instrument Along the Traverse of the Curiosity Rover, Gale Crater, Mars, in: Lunar and Planetary Science Conference. Presented at the Lunar and Planetary Science Conference.

Grotzinger, J.P., Gupta, S., Malin, M.C., Rubin, D.M., Schieber, J., Siebach, K., Sumner, D.Y., Stack, K.M., Vasavada, A.R., Arvidson, R.E., Calef, F., Edgar, L., Fischer, W.F., Grant, J.A., Griffes, J., Kah, L.C., Lamb, M.P., Lewis, K.W., Mangold, N., Minitti, M.E., Palucis, M., Rice, M., Williams, R.M.E., Yingst, R.A., Blake, D., Blaney, D., Conrad, P., Crisp, J.,

Dietrich, W.E., Dromart, G., Edgett, K.S., Ewing, R.C., Gellert, R., Hurowitz, J.A., Kocurek, G., Mahaffy, P., McBride, M.J., McLennan, S.M., Mischna, M., Ming, D., Milliken, R., Newsom, H., Oehler, D., Parker, T.J., Vaniman, D., Wiens, R.C., Wilson, S.A., 2015. Deposition, exhumation, and paleoclimate of an ancient lake deposit, Gale crater, Mars. Science 350, aac7575-aac7575. https://doi.org/10.1126/science.aac7575

Guilbert, J.M., Park, C.F., 2007. The Geology of Ore Deposits. Waveland Press.

Hahn, B.C., McLennan, S.M., 2007. Evolution and Geochemistry of the Martian Crust: Integrating Mission Datasets, in: Seventh International Conference on Mars. Presented at the Seventh International Conference on Mars, p. 3179.

Hardgrove, C., Johnson, J., Rice, M., Bell, J., Kinch, K., Wellington, D., Arvidson, R., Godber, A., 2015. Detecting High Manganese Phases in Curiosity Mastcam Multispectral Images and Chemcam Passive Visible to Near Infrared Spectra. Presented at the Lunar and Planetary Science Conference, p. 2748.

Henley, R.W., Berger, B.R., 2012. Pyrite–sulfosalt reactions and semimetal fractionation in the Chinkuashih, Taiwan, copper–gold deposit: a 1 Ma paleo-fumarole. Geofluids 12, 245–260. https://doi.org/10.1111/j.1468-8123.2012.00367.x

Herd, C.D.K., 2003. The oxygen fugacity of olivine-phyric martian basalts and the components within the mantle and crust of Mars. Meteorit. Planet. Sci. 38, 1793–1805. https://doi.org/10.1111/j.1945-5100.2003.tb00015.x

Hurowitz, J.A., Grotzinger, J.P., Fischer, W.W., McLennan, S.M., Milliken, R.E., Stein, N., Vasavada, A.R., Blake, D.F., Dehouck, E., Eigenbrode, J.L., Fairén, A.G., Frydenvang, J., Gellert, R., Grant, J.A., Gupta, S., Herkenhoff, K.E., Ming, D.W., Rampe, E.B., Schmidt, M.E., Siebach, K.L., Stack-Morgan, K., Sumner, D.Y., Wiens, R.C., 2017. Redox stratification of an ancient lake in Gale crater, Mars. Science 356, eaah6849. https://doi.org/10.1126/science.aah6849

Karunatillake, S., Wray, J.J., Gasnault, O., McLennan, S.M., Rogers, A.D., Squyres, S.W., Boynton, W.V., Skok, J.R., Ojha, L., Olsen, N., 2014. Sulfates hydrating bulk soil in the Martian low and middle latitudes. Geophys. Res. Lett. 41, 7987–7996. https://doi.org/10.1002/2014GL061136

Lanza, N.L., Fischer, W.W., Wiens, R.C., Grotzinger, J., Ollila, A.M., Cousin, A., Anderson, R.B., Clark, B.C., Gellert, R., Mangold, N., Maurice, S., Le Mouélic, S., Nachon, M., Schmidt, M., Berger, J., Clegg, S.M., Forni, O., Hardgrove, C., Melikechi, N., Newsom, H.E., Sautter, V., 2014. High manganese concentrations in rocks at Gale crater, Mars. Geophys. Res. Lett. 41, 5755–5763. https://doi.org/10.1002/2014GL060329

Lanza, N.L., Wiens, R.C., Arvidson, R.E., Clark, B.C., Fischer, W.W., Gellert, R., Grotzinger, J.P., Hurowitz, J.A., McLennan, S.M., Morris, R.V., Rice, M.S., Bell, J.F., Berger, J.A., Blaney, D.L., Bridges, N.T., Calef, F., Campbell, J.L., Clegg, S.M., Cousin, A., Edgett, K.S., Fabre, C., Fisk, M.R., Forni, O., Frydenvang, J., Hardy, K.R., Hardgrove, C., Johnson, J.R., Lasue, J., Le Mouélic, S., Malin, M.C., Mangold, N., Martìn-Torres, J., Maurice, S., McBride, M.J., Ming, D.W., Newsom, H.E., Ollila, A.M., Sautter, V., Schröder, S., Thompson, L.M., Treiman, A.H., VanBommel, S., Vaniman, D.T., Zorzano, M.-P., 2016. Oxidation of manganese in an ancient aquifer, Kimberley formation, Gale crater, Mars: Manganese Fracture Fills in Gale Crater. Geophys. Res. Lett. 43, 7398–7407. https://doi.org/10.1002/2016GL069109

Lasue, J., Clegg, S.M., Forni, O., Cousin, A., Wiens, R.C., Lanza, N., Mangold, N., Le Deit, L., Gasnault, O., Maurice, S., Berger, J.A., Stack, K., Blaney, D., Fabre, C., Goetz, W., Johnson, J., Le Mouélic, S., Nachon, M., Payré, V., Rapin, W., Sumner, D.Y., 2016. Observation of > 5 wt % zinc at the Kimberley outcrop, Gale crater, Mars. J. Geophys. Res. Planets 121, 2015JE004946. https://doi.org/10.1002/2015JE004946

Laznicka, P., 2010. Giant Metallic Deposits: Future Sources of Industrial Metals. Springer

Science & Business Media.

Le Deit, L., Mangold, N., Forni, O., Cousin, A., Lasue, J., Schröder, S., Wiens, R.C., Sumner, D., Fabre, C., Stack, K.M., Anderson, R.B., Blaney, D., Clegg, S., Dromart, G., Fisk, M., Gasnault, O., Grotzinger, J.P., Gupta, S., Lanza, N., Le Mouélic, S., Maurice, S., McLennan, S.M., Meslin, P.-Y., Nachon, M., Newsom, H., Payré, V., Rapin, W., Rice, M., Sautter, V., Treiman, A.H., 2016. The potassic sedimentary rocks in Gale Crater, Mars, as seen by ChemCam on board Curiosity. J. Geophys. Res. Planets 121, 2015JE004987. https://doi.org/10.1002/2015JE004987

Le Mouélic, S., Gasnault, O., Herkenhoff, K.E., Bridges, N.T., Langevin, Y., Mangold, N., Maurice, S., Wiens, R.C., Pinet, P., Newsom, H.E., Deen, R.G., Bell, J.F., Johnson, J.R., Rapin, W., Barraclough, B., Blaney, D.L., Deflores, L., Maki, J., Malin, M.C., Pérez, R., Saccoccio, M., 2015. The ChemCam Remote Micro-Imager at Gale crater: Review of the first year of operations on Mars. Icarus 249, 93–107. https://doi.org/10.1016/j.icarus.2014.05.030

Lorand, J.-P., Chevrier, V., Sautter, V., 2005. Sulfide mineralogy and redox conditions in some shergottites. Meteorit. Planet. Sci. 40, 1257–1272. https://doi.org/10.1111/j.1945-5100.2005.tb00187.x

Lowell, J.D., Guilbert, J.M., 1970. Lateral and vertical alteration-mineralization zoning in porphyry ore deposits. Econ. Geol. 65, 373–408. https://doi.org/10.2113/gsecongeo.65.4.373

Manceau, A., Lanson, M., Geoffroy, N., 2007. Natural speciation of Ni, Zn, Ba, and As in ferromanganese coatings on quartz using X-ray fluorescence, absorption, and diffraction. Geochim. Cosmochim. Acta 71, 95–128. https://doi.org/10.1016/j.gca.2006.08.036

Mangold, N., Forni, O., Dromart, G., Stack, K., Wiens, R.C., Gasnault, O., Sumner, D.Y., Nachon, M., Meslin, P.-Y., Anderson, R.B., Barraclough, B., Bell, J.F., Berger, G., Blaney, D.L., Bridges, J.C., Calef, F., Clark, B., Clegg, S.M., Cousin, A., Edgar, L., Edgett, K., Ehlmann, B., Fabre, C., Fisk, M., Grotzinger, J., Gupta, S., Herkenhoff, K.E., Hurowitz, J.,

Johnson, J.R., Kah, L.C., Lanza, N., Lasue, J., Le Mouélic, S., Léveillé, R., Lewin, E., Malin, M., McLennan, S., Maurice, S., Melikechi, N., Mezzacappa, A., Milliken, R., Newsom, H., Ollila, A., Rowland, S.K., Sautter, V., Schmidt, M., Schröder, S., d'Uston, C., Vaniman, D., Williams, R., 2015. Chemical variations in Yellowknife Bay formation sedimentary rocks analyzed by ChemCam on board the Curiosity rover on Mars. J. Geophys. Res. Planets 120, 452–482. https://doi.org/10.1002/2014JE004681

Maurice, S., Clegg, S.M., Wiens, R.C., Gasnault, O., Rapin, W., Forni, O., Cousin, A., Sautter, V., Mangold, N., Deit, L.L., Nachon, M., Anderson, R.B., Lanza, N.L., Fabre, C., Payré, V., Lasue, J., Meslin, P.-Y., Léveillé, R.J., Barraclough, B.L., Beck, P., Bender, S.C., Berger, G., Bridges, J.C., Bridges, N.T., Dromart, G., Dyar, M.D., Francis, R., Frydenvang, J., Gondet, B., Ehlmann, B.L., Herkenhoff, K.E., Johnson, J.R., Langevin, Y., Madsen, M.B., Melikechi, N., Lacour, J.-L., Mouélic, S.L., Lewin, E., Newsom, H.E., Ollila, A.M., Pinet, P., Schröder, S., Sirven, J.-B., Tokar, R.L., Toplis, M.J., d'Uston, C., Vaniman, D.T., Vasavada, A.R., 2016. ChemCam activities and discoveries during the nominal mission of the Mars Science Laboratory in Gale crater, Mars. J. Anal. At. Spectrom. 31, 863–889. https://doi.org/10.1039/C5JA00417A

Maurice, S., Wiens, R.C., Saccoccio, M., Barraclough, B., Gasnault, O., Forni, O., Mangold, N., Baratoux, D., Bender, S., Berger, G., Bernardin, J., Berthé, M., Bridges, N., Blaney, D., Bouyé, M., Caïs, P., Clark, B., Clegg, S., Cousin, A., Cremers, D., Cros, A., DeFlores, L., Derycke, C., Dingler, B., Dromart, G., Dubois, B., Dupieux, M., Durand, E., d'Uston, L., Fabre, C., Faure, B., Gaboriaud, A., Gharsa, T., Herkenhoff, K., Kan, E., Kirkland, L., Kouach, D., Lacour, J.-L., Langevin, Y., Lasue, J., Le Mouélic, S., Lescure, M., Lewin, E., Limonadi, D., Manhès, G., Mauchien, P., McKay, C., Meslin, P.-Y., Michel, Y., Miller, E., Newsom, H.E., Orttner, G., Paillet, A., Parès, L., Parot, Y., Pérez, R., Pinet, P., Poitrasson, F., Quertier, B., Sallé, B., Sotin, C., Sautter, V., Séran, H., Simmonds, J.J., Sirven, J.-B., Stiglich,

R., Striebig, N., Thocaven, J.-J., Toplis, M.J., Vaniman, D., 2012. The ChemCam Instrument Suite on the Mars Science Laboratory (MSL) Rover: Science Objectives and Mast Unit Description. Space Sci. Rev. 170, 95–166. https://doi.org/10.1007/s11214-012-9912-2

McCubbin, F.M., Hauri, E.H., Elardo, S.M., Kaaden, K.E.V., Wang, J., Shearer, C.K., 2012. Hydrous melting of the martian mantle produced both depleted and enriched shergottites. Geology 40, 683–686. https://doi.org/10.1130/G33242.1

McLennan, S.M., 2001. Relationships between the trace element composition of sedimentary rocks and upper continental crust: trace element composition and upper continental crust. Geochem. Geophys. Geosystems 2, n/a-n/a. https://doi.org/10.1029/2000GC000109

McLennan, S.M., Anderson, R.B., Bell, J.F., Bridges, J.C., Calef, F., Campbell, J.L., Clark, B.C., Clegg, S., Conrad, P., Cousin, A., Des Marais, D.J., Dromart, G., Dyar, M.D., Edgar, L.A., Ehlmann, B.L., Fabre, C., Forni, O., Gasnault, O., Gellert, R., Gordon, S., Grant, J.A., Grotzinger, J.P., Gupta, S., Herkenhoff, K.E., Hurowitz, J.A., King, P.L., Le Mouelic, S., Leshin, L.A., Leveille, R., Lewis, K.W., Mangold, N., Maurice, S., Ming, D.W., Morris, R.V., Nachon, M., Newsom, H.E., Ollila, A.M., Perrett, G.M., Rice, M.S., Schmidt, M.E., Schwenzer, S.P., Stack, K., Stolper, E.M., Sumner, D.Y., Treiman, A.H., VanBommel, S., Vaniman, D.T., Vasavada, A., Wiens, R.C., Yingst, R.A., MSL Science Team, Kemppinen, O., Bridges, N., Johnson, J.R., Minitti, M., Cremers, D., Farmer, J., Godber, A., Wadhwa, M., Wellington, D., McEwan, I., Newman, C., Richardson, M., Charpentier, A., Peret, L., Blank, J., Weigle, G., Li, S., Milliken, R., Robertson, K., Sun, V., Baker, M., Edwards, C., Farley, K., Griffes, J., Miller, H., Newcombe, M., Pilorget, C., Siebach, K., Brunet, C., Hipkin, V., Marchand, G., Sanchez, P.S., Favot, L., Cody, G., Steele, A., Fluckiger, L., Lees, D., Nefian, A., Martin, M., Gailhanou, M., Westall, F., Israel, G., Agard, C., Baroukh, J., Donny, C., Gaboriaud, A., Guillemot, P., Lafaille, V., Lorigny, E., Paillet, A., Perez, R., Saccoccio, M., Yana, C., Armiens-Aparicio, C., Rodriguez, J.C., Blazquez, I.C., Gomez, F.G., Gomez-Elvira,

J., Hettrich, S., Malvitte, A.L., Jimenez, M.M., Martinez-Frias, J., Martin-Soler, J., Martin-Torres, F.J., Jurado, A.M., Mora-Sotomayor, L., Caro, G.M., Lopez, S.N., Peinado-Gonzalez, V., Pla-Garcia, J., Manfredi, J.A.R., Romeral-Planello, J.J., Fuentes, S.A.S., Martinez, E.S., Redondo, J.T., Urqui-O'Callaghan, R., Mier, M.-P.Z., Chipera, S., Lacour, J.-L., Mauchien, P., Sirven, J.-B., Manning, H., Fairen, A., Hayes, A., Joseph, J., Squyres, S., Sullivan, R., Thomas, P., Dupont, A., Lundberg, A., Melikechi, N., Mezzacappa, A., DeMarines, J., Grinspoon, D., Reitz, G., Prats, B., Atlaskin, E., Genzer, M., Harri, A.-M., Haukka, H., Kahanpaa, H., Kauhanen, J., Kemppinen, O., Paton, M., Polkko, J., Schmidt, W., Siili, T., Wray, J., Wilhelm, M.B., Poitrasson, F., Patel, K., Gorevan, S., Indyk, S., Paulsen, G., Bish, D., Schieber, J., Gondet, B., Langevin, Y., Geffroy, C., Baratoux, D., Berger, G., Cros, A., d'Uston, C., Lasue, J., Lee, Q.-M., Meslin, P.-Y., Pallier, E., Parot, Y., Pinet, P., Schroder, S., Toplis, M., Lewin, E., Brunner, W., Heydari, E., Achilles, C., Oehler, D., Sutter, B., Cabane, M., Coscia, D., Israel, G., Szopa, C., Robert, F., Sautter, V., Buch, A., Stalport, F., Coll, P., Francois, P., Raulin, F., Teinturier, S., Cameron, J., DeLapp, D., Dingler, R., Jackson, R.S., Johnstone, S., Lanza, N., Little, C., Nelson, T., Williams, R.B., Jones, A., Kirkland, L., Baker, B., Cantor, B., Caplinger, M., Davis, S., Duston, B., Edgett, K., Fay, D., Hardgrove, C., Harker, D., Herrera, P., Jensen, E., Kennedy, M.R., Krezoski, G., Krysak, D., Lipkaman, L., Malin, M., McCartney, E., McNair, S., Nixon, B., Posiolova, L., Ravine, M., Salamon, A., Saper, L., Stoiber, K., Supulver, K., Van Beek, J., Van Beek, T., Zimdar, R., French, K.L., Iagnemma, K., Miller, K., Summons, R., Goesmann, F., Goetz, W., Hviid, S., Johnson, M., Lefavor, M., Lyness, E., Breves, E., Fassett, C., Blake, D.F., Bristow, T., Edwards, L., Haberle, R., Hoehler, T., Hollingsworth, J., Kahre, M., Keely, L., McKay, C., Wilhelm, M.B., Bleacher, L., Brinckerhoff, W., Choi, D., Dworkin, J.P., Eigenbrode, J., Floyd, M., Freissinet, C., Garvin, J., Glavin, D., Harpold, D., Jones, A., Mahaffy, P., Martin, D.K., McAdam, A., Pavlov, A., Raaen, E., Smith, M.D., Stern, J., Tan, F., Trainer, M., Meyer, M., Posner, A.,

Voytek, M., Anderson, R.C., Aubrey, A., Beegle, L.W., Behar, A., Blaney, D., Brinza, D., Christensen, L., Crisp, J.A., DeFlores, L., Ehlmann, B., Feldman, J., Feldman, S., Flesch, G., Jun, I., Keymeulen, D., Maki, J., Mischna, M., Morookian, J.M., Parker, T., Pavri, B., Schoppers, M., Sengstacken, A., Simmonds, J.J., Spanovich, N., Juarez, M. d. l. T., Webster, C.R., Yen, A., Archer, P.D., Cucinotta, F., Jones, J.H., Niles, P., Rampe, E., Nolan, T., Fisk, M., Radziemski, L., Barraclough, B., Bender, S., Berman, D., Dobrea, E.N., Tokar, R., Williams, R.M.E., Cleghorn, T., Huntress, W., Manhes, G., Hudgins, J., Olson, T., Stewart, N., Sarrazin, P., Vicenzi, E., Wilson, S.A., Bullock, M., Ehresmann, B., Hamilton, V., Hassler, D., Peterson, J., Rafkin, S., Zeitlin, C., Fedosov, F., Golovin, D., Karpushkina, N., Kozyrev, A., Litvak, M., Malakhov, A., Mitrofanov, I., Mokrousov, M., Nikiforov, S., Prokhorov, V., Sanin, A., Tretyakov, V., Varenikov, A., Vostrukhin, A., Kuzmin, R., Wolff, M., Botta, O., Drake, D., Bean, K., Lemmon, M., Lee, E.M., Sucharski, R., Hernandez, M.A. d. P., Avalos, J.J.B., Ramos, M., Kim, M.-H., Malespin, C., Plante, I., Muller, J.-P., Navarro-Gonzalez, R., Ewing, R., Boynton, W., Downs, R., Fitzgibbon, M., Harshman, K., Morrison, S., Dietrich, W., Kortmann, O., Palucis, M., Williams, A., Lugmair, G., Wilson, M.A., Rubin, D., Jakosky, B., Balic-Zunic, T., Frydenvang, J., Jensen, J.K., Kinch, K., Koefoed, A., Madsen, M.B., Stipp, S.L.S., Boyd, N., Pradler, I., Jacob, S., Owen, T., Rowland, S., Atlaskin, E., Savijarvi, H., Boehm, E., Bottcher, S., Burmeister, S., Guo, J., Kohler, J., Garcia, C.M., Mueller-Mellin, R., Wimmer-Schweingruber, R., McConnochie, T., Benna, M., Franz, H., Bower, H., Brunner, A., Blau, H., Boucher, T., Carmosino, M., Atreya, S., Elliott, H., Halleaux, D., Renno, N., Wong, M., Pepin, R., Elliott, B., Spray, J., Thompson, L., Williams, J., Vasconcelos, P., Bentz, J., Nealson, K., Popa, R., Kah, L.C., Moersch, J., Tate, C., Day, M., Kocurek, G., Hallet, B., Sletten, R., Francis, R., McCullough, E., Cloutis, E., ten Kate, I.L., Kuzmin, R., Arvidson, R., Fraeman, A., Scholes, D., Slavney, S., Stein, T., Ward, J., Berger, J., Moores, J.E., 2014. Elemental Geochemistry of Sedimentary Rocks at Yellowknife

Bay, Gale Crater, Mars. Science 343, 1244734–1244734. https://doi.org/10.1126/science.1244734

McLennan, S.M., Boynton, W.V., Karunatillake, S., Hahn, B.C., Taylor, G.J., Team, M.O.G., 2010. Distribution of Sulfur on the Surface of Mars Determined by the 2001 Mars Odyssey Gamma Ray Spectrometer, in: Lunar and Planetary Science Conference. Presented at the Lunar and Planetary Science Conference, p. 2174.

McSween, H.Y., 1994. What we have learned about Mars from SNC meteorites. Meteoritics 29, 757–779. https://doi.org/10.1111/j.1945-5100.1994.tb01092.x

McSween, H.Y., Grove, T.L., Lentz, R.C.F., Dann, J.C., Holzheid, A.H., Riciputi, L.R., Ryan, J.G., 2001. Geochemical evidence for magmatic water within Mars from pyroxenes in the Shergotty meteorite. Nature 409, 487–490. https://doi.org/10.1038/35054011

Morrison, S.M., Downs, R.T., Blake, D.F., Vaniman, D.T., Ming, D.W., Hazen, R.M., Treiman, A.H., Achilles, C.N., Yen, A.S., Morris, R.V., Rampe, E.B., Bristow, T.F., Chipera, S.J., Sarrazin, P.C., Gellert, R., Fendrich, K.V., Morookian, J.M., Farmer, J.D., Marais, D.J.D., Craig, P.I., 2018. Crystal chemistry of martian minerals from Bradbury Landing through Naukluft Plateau, Gale crater, Mars. Am. Mineral. 103, 857–871. https://doi.org/10.2138/am-2018-6124

Murray, J.W., 1975. The interaction of metal ions at the manganese dioxide-solution interface. Geochim. Cosmochim. Acta 39, 505–519. https://doi.org/10.1016/0016-7037(75)90103-9

Nachon, M., Clegg, S.M., Mangold, N., Schröder, S., Kah, L.C., Dromart, G., Ollila, A., Johnson, J.R., Oehler, D.Z., Bridges, J.C., Le Mouélic, S., Forni, O., Wiens, R.C., Anderson, R.B., Blaney, D.L., Bell, J.F., Clark, B., Cousin, A., Dyar, M.D., Ehlmann, B., Fabre, C., Gasnault, O., Grotzinger, J., Lasue, J., Lewin, E., Léveillé, R., McLennan, S., Maurice, S., Meslin, P.-Y., Rapin, W., Rice, M., Squyres, S.W., Stack, K., Sumner, D.Y., Vaniman, D.,

Wellington, D., 2014. Calcium sulfate veins characterized by ChemCam/Curiosity at Gale crater, Mars. J. Geophys. Res. Planets 119, 1991–2016. https://doi.org/10.1002/2013JE004588

Nachon, M., Mangold, N., Forni, O., Kah, L.C., Cousin, A., Wiens, R.C., Anderson, R., Blaney, D., Blank, J.G., Calef, F., Clegg, S.M., Fabre, C., Fisk, M.R., Gasnault, O., Grotzinger, J.P., Kronyak, R., Lanza, N.L., Lasue, J., Deit, L.L., Mouélic, S.L., Maurice, S., Meslin, P.-Y., Oehler, D.Z., Payré, V., Rapin, W., Schröder, S., Stack, K., Sumner, D., 2017. Chemistry of diagenetic features analyzed by ChemCam at Pahrump Hills, Gale crater, Mars. Icarus 281, 121–136. https://doi.org/10.1016/j.icarus.2016.08.026

Newsom, H.E., Brittelle, G.E., Hibbitts, C.A., Crossey, L.J., Kudo, A.M., 1996. Impact crater lakes on Mars. J. Geophys. Res. Planets 101, 14951–14955. https://doi.org/10.1029/96JE01139

Ollila, A.M., Newsom, H.E., Clark, B., Wiens, R.C., Cousin, A., Blank, J.G., Mangold, N., Sautter, V., Maurice, S., Clegg, S.M., Gasnault, O., Forni, O., Tokar, R., Lewin, E., Dyar, M.D., Lasue, J., Anderson, R., McLennan, S.M., Bridges, J., Vaniman, D., Lanza, N., Fabre, C., Melikechi, N., Perrett, G.M., Campbell, J.L., King, P.L., Barraclough, B., Delapp, D., Johnstone, S., Meslin, P.-Y., Rosen-Gooding, A., Williams, J., The MSL Science Team, 2014. Trace element geochemistry (Li, Ba, Sr, and Rb) using *Curiosity* 's ChemCam: Early results for Gale crater from Bradbury Landing Site to Rocknest. J. Geophys. Res. Planets 119, 255–285. https://doi.org/10.1002/2013JE004517

Osinski, G.R., Lee, P., Parnell, J., Spray, J.G., Baron, M., 2005. A case study of impact-induced hydrothermal activity: The Haughton impact structure, Devon Island, Canadian High Arctic. Meteorit. Planet. Sci. 40, 1859–1877. https://doi.org/10.1111/j.1945-5100.2005.tb00150.x

Osinski, G.R., Spray, J.G., Lee, P., 2001. Impact-induced hydrothermal activity within the

Haughton impact structure, arctic Canada: Generation of a transient, warm, wet oasis. Meteorit. Planet. Sci. 36, 731–745. https://doi.org/10.1111/j.1945-5100.2001.tb01910.x

Palucis, M.C., Dietrich, W.E., Hayes, A.G., Williams, R.M.E., Gupta, S., Mangold, N., Newsom, H., Hardgrove, C., Calef, F., Sumner, D.Y., 2014. The origin and evolution of the Peace Vallis fan system that drains to the *Curiosity* landing area, Gale Crater, Mars: Origin and evolution of Peace Vallis fan. J. Geophys. Res. Planets 119, 705–728. https://doi.org/10.1002/2013JE004583

Payré, V., Fabre, C., Cousin, A., Sautter, V., Wiens, R.C., Forni, O., Gasnault, O., Mangold, N., Meslin, P.-Y., Lasue, J., Ollila, A., Rapin, W., Maurice, S., Nachon, M., Le Deit, L., Lanza, N., Clegg, S., 2017. Alkali trace elements in Gale crater, Mars, with ChemCam: Calibration update and geological implications. J. Geophys. Res. Planets 2016JE005201. https://doi.org/10.1002/2016JE005201

Richards, J., 2016. Economic geology: Clues to hidden copper deposits. Nat. Geosci. 9, 195–196. https://doi.org/10.1038/ngeo2656

Richards, J.P., 2009. Postsubduction porphyry Cu-Au and epithermal Au deposits: Products of remelting of subduction-modified lithosphere. Geology 37, 247–250. https://doi.org/10.1130/G25451A.1

Ridley, J., 2013. Ore Deposit Geology. Cambridge University Press, Cambridge. https://doi.org/10.1017/CBO9781139135528

Righter, K., Pando, K., Danielson, L.R., 2009. Experimental evidence for sulfur-rich martian magmas: Implications for volcanism and surficial sulfur sources. Earth Planet. Sci. Lett. 288, 235–243. https://doi.org/10.1016/j.epsl.2009.09.027

Rochette, P., Lorand, J.-P., Fillion, G., Sautter, V., 2001. Pyrrhotite and the remanent magnetization of SNC meteorites: a changing perspective on Martian magnetism. Earth Planet. Sci. Lett. 190, 1–12. https://doi.org/10.1016/S0012-821X(01)00373-9

Rudnick, R.L., Gao, S., 2003. Composition of the Continental Crust, in: Treatise on Geochemistry. Elsevier, pp. 1–64. https://doi.org/10.1016/B0-08-043751-6/03016-4

Sautter, V., Cousin, A., Dromard, G., Fabre, C., Forni, O., Gasnault, O., Le Mouélic, S., Mangold, N., Maurice, S., Minitti, M.E., Newson, H.E., Pinet, P., Schieber, J., Toplis, M., Wiens, R.C., Team, M.S.L., 2013. Is Bathurst Inlet Rock an Evidence of Explosive Volcanism in the Rocknest Area of Gale Crater?, in: Lunar and Planetary Science Conference. Presented at the Lunar and Planetary Science Conference, p. 1985.

Sautter, V., Toplis, M.J., Beck, P., Mangold, N., Wiens, R., Pinet, P., Cousin, A., Maurice, S., LeDeit, L., Hewins, R., Gasnault, O., Quantin, C., Forni, O., Newsom, H., Meslin, P.-Y., Wray, J., Bridges, N., Payré, V., Rapin, W., Le Mouélic, S., 2016. Magmatic complexity on early Mars as seen through a combination of orbital, in-situ and meteorite data. Lithos 254–255, 36–52. https://doi.org/10.1016/j.lithos.2016.02.023

Sautter, V., Toplis, M.J., Wiens, R.C., Cousin, A., Fabre, C., Gasnault, O., Maurice, S., Forni, O., Lasue, J., Ollila, A., Bridges, J.C., Mangold, N., Le Mouélic, S., Fisk, M., Meslin, P.-Y., Beck, P., Pinet, P., Le Deit, L., Rapin, W., Stolper, E.M., Newsom, H., Dyar, D., Lanza, N., Vaniman, D., Clegg, S., Wray, J.J., 2015. In situ evidence for continental crust on early Mars. Nat. Geosci. 8, 605–609. https://doi.org/10.1038/ngeo2474

Schmidt, M.E., King, P.L., Gellert, R., Elliott, B., Thompson, L., Berger, J.A., Bridges, J.C., Campbell, J.L., Ehlmann, B.L., Grotzinger, J., Hurowitz, J.A., Leshin, L.A., Lewis, K.W., McLennan, S.M., Ming, D.W., Perrett, G., Pradler, I., Stolper, E.M., Squyres, S.W., Treiman, A.H., MSL Science Team, 2013. APXS of First Rocks Encountered by Curiosity in Gale Crater: Geochemical Diversity and Volatile Element (K and Zn) Enrichment. Presented at the Lunar and Planetary Science Conference, p. 1278.

Schwenzer, S.P., Abramov, O., Allen, C.C., Bridges, J.C., Clifford, S.M., Filiberto, J., Kring, D.A., Lasue, J., McGovern, P.J., Newsom, H.E., Treiman, A.H., Vaniman, D.T., Wiens, R.C.,

Wittmann, A., 2012. Gale Crater: Formation and post-impact hydrous environments. Planet. Space Sci. 70, 84–95. https://doi.org/10.1016/j.pss.2012.05.014

Schwenzer, S.P., Kring, D.A., 2009. Impact-generated hydrothermal systems capable of forming phyllosilicates on Noachian Mars. Geology 37, 1091–1094. https://doi.org/10.1130/G30340A.1

Shanks, W.C.P., Thurston, R., 2012. Volcanogenic Massive Sulfide Occurrence Model. Econ. Geol. 107, 1073–1073. https://doi.org/10.2113/econgeo.107.5.1073

Sheridan, M.F., 1970. Fuarmolic Mounds and Ridges of the Bishop Tuff, California. Geol. Soc. Am. Bull. 81, 851. https://doi.org/10.1130/0016-7606(1970)81[851:FMAROT]2.0.CO;2

Sillitoe, R.H., 2010. Porphyry Copper Systems. Econ. Geol. 105, 3–41. https://doi.org/10.2113/gsecongeo.105.1.3

Slack John, F., P, F.M., K, F.M.J., V, S.M., E, B.H., 2003. Exhalative subsea-floor replacement processes in the formation of the Bald Mountain massive sulfide deposit, northern Maine [WWW Document]. Econ. Geol. Monogr. URL https://eurekamag.com/research/018/886/018886934.php (accessed 6.21.17).

Sluzhenikin, S.F., Krivolutskaya, N.A., Rad'ko, V.A., Malitch, K.N., Distler, V.V., Fedorenko, V.A., 2014. Ultramafic-mafic intrusions, volcanic rocks and PGE-Cu-Ni sulfide deposits of the Noril'sk Province, Polar Siberia EPUB Derniers Ebooks Free Download, Simonov, O.N. ed. 12th International platinum symposium, Yekaterinburg, Russia.

Stack, K.M., Edwards, C.S., Grotzinger, J.P., Gupta, S., Sumner, D.Y., Calef, F.J., Edgar, L.A., Edgett, K.S., Fraeman, A.A., Jacob, S.R., Le Deit, L., Lewis, K.W., Rice, M.S., Rubin, D., Williams, R.M.E., Williford, K.H., 2016. Comparing orbiter and rover image-based mapping of an ancient sedimentary environment, Aeolis Palus, Gale crater, Mars. Icarus 280, 3–21. https://doi.org/10.1016/j.icarus.2016.02.024

Taylor, S.R., McLennan, S., 2009. Planetary Crusts: Their Composition, Origin and

Evolution. Cambridge University Press, Cambridge. https://doi.org/10.1017/CBO9780511575358

Thomas, E., Varekamp, J.C., Buseck, P.R., 1982. Zinc enrichment in the phreatic ashes of Mt. St. Helens, April 1980. J. Volcanol. Geotherm. Res. 12, 339–350. https://doi.org/10.1016/0377-0273(82)90033-6

Thompson, L.M., Schmidt, M.E., Spray, J.G., Berger, J.A., Fairén, A.G., Campbell, J.L., Perrett, G.M., Boyd, N., Gellert, R., Pradler, I., VanBommel, S.J., 2016. Potassium-rich sandstones within the Gale impact crater, Mars: The APXS perspective: Potassium-Rich Sandstones on Mars. J. Geophys. Res. Planets 121, 1981–2003. https://doi.org/10.1002/2016JE005055

Tourtelot, E.B., Vine, J.D., 1976. Copper Deposits in Sedimentary and Volcanogenic Rocks (No. 907–C). U.S. Geological Survey.

Treiman, A.H., Bish, D.L., Vaniman, D.T., Chipera, S.J., Blake, D.F., Ming, D.W., Morris, R.V., Bristow, T.F., Morrison, S.M., Baker, M.B., Rampe, E.B., Downs, R.T., Filiberto, J., Glazner, A.F., Gellert, R., Thompson, L.M., Schmidt, M.E., Le Deit, L., Wiens, R.C., McAdam, A.C., Achilles, C.N., Edgett, K.S., Farmer, J.D., Fendrich, K.V., Grotzinger, J.P., Gupta, S., Morookian, J.M., Newcombe, M.E., Rice, M.S., Spray, J.G., Stolper, E.M., Sumner, D.Y., Vasavada, A.R., Yen, A.S., 2016. Mineralogy, provenance, and diagenesis of a potassic basaltic sandstone on Mars: CheMin X-ray diffraction of the Windjana sample (Kimberley area, Gale Crater). J. Geophys. Res. Planets 121, 75–106. https://doi.org/10.1002/2015JE004932

Tuff, J., Wade, J., Wood, B.J., 2013. Volcanism on Mars controlled by early oxidation of the upper mantle. Nature 498, 342–345. https://doi.org/10.1038/nature12225

Wang, Z., Becker, H., 2017. Chalcophile elements in Martian meteorites indicate low sulfur content in the Martian interior and a volatile element-depleted late veneer. Earth Planet. Sci.

Lett. 463, 56–68. https://doi.org/10.1016/j.epsl.2017.01.023

White, W.M., Klein, E.M., 2014. Composition of the Oceanic Crust, in: Treatise on Geochemistry. Elsevier, pp. 457–496. https://doi.org/10.1016/B978-0-08-095975-7.00315-6

Wiens, R.C., Mangold, N., Gasnault, O., Payré, V., Stack, K.M., House, C., Fedo, C., Edgett, K.S., Watkins, J., Grotzinger, J.P., Gupta, S., Frydenvang, J., Gasda, P., Leveille, R., Maurice, S., Johnstone, S., 2017. Bimbe and Related Blocky Geomorphic Units in Gale Crater: Heterogeneous Compositional Units Overlying Murray and Stimson Formations, in: Lunar and Planetary Science Conference. Presented at the Lunar and Planetary Science Conference, p. 2573.

Wiens, R.C., Maurice, S., Barraclough, B., Saccoccio, M., Barkley, W.C., Bell, J.F., Bender, S., Bernardin, J., Blaney, D., Blank, J., Bouyé, M., Bridges, N., Bultman, N., Caïs, P., Clanton, R.C., Clark, B., Clegg, S., Cousin, A., Cremers, D., Cros, A., DeFlores, L., Delapp, D., Dingler, R., D'Uston, C., Darby Dyar, M., Elliott, T., Enemark, D., Fabre, C., Flores, M., Forni, O., Gasnault, O., Hale, T., Hays, C., Herkenhoff, K., Kan, E., Kirkland, L., Kouach, D., Landis, D., Langevin, Y., Lanza, N., LaRocca, F., Lasue, J., Latino, J., Limonadi, D., Lindensmith, C., Little, C., Mangold, N., Manhes, G., Mauchien, P., McKay, C., Miller, E., Mooney, J., Morris, R.V., Morrison, L., Nelson, T., Newsom, H., Ollila, A., Ott, M., Pares, L., Perez, R., Poitrasson, F., Provost, C., Reiter, J.W., Roberts, T., Romero, F., Sautter, V., Salazar, S., Simmonds, J.J., Stiglich, R., Storms, S., Striebig, N., Thocaven, J.-J., Trujillo, T., Ulibarri, M., Vaniman, D., Warner, N., Waterbury, R., Whitaker, R., Witt, J., Wong-Swanson, B., 2012. The ChemCam Instrument Suite on the Mars Science Laboratory (MSL) Rover: Body Unit and Combined System Tests. Space Sci. Rev. 170, 167–227. https://doi.org/10.1007/s11214-012-9902-4

Wiens, R.C., Maurice, S., Lasue, J., Forni, O., Anderson, R.B., Clegg, S., Bender, S., Blaney, D., Barraclough, B.L., Cousin, A., Deflores, L., Delapp, D., Dyar, M.D., Fabre, C., Gasnault,

O., Lanza, N., Mazoyer, J., Melikechi, N., Meslin, P.-Y., Newsom, H., Ollila, A., Perez, R., Tokar, R.L., Vaniman, D., 2013. Pre-flight calibration and initial data processing for the ChemCam laser-induced breakdown spectroscopy instrument on the Mars Science Laboratory rover. Spectrochim. Acta Part B At. Spectrosc. 82, 1–27. https://doi.org/10.1016/j.sab.2013.02.003

Wiens, R.C., Maurice, S., MSL Science Team, 2015. ChemCam: Chemostratigraphy by the First Mars Microprobe. Elements 11, 33–38. https://doi.org/10.2113/gselements.11.1.33

Williams-Jones, A.E., Heinrich, C.A., 2005. 100th Anniversary Special Paper: Vapor Transport of Metals and the Formation of Magmatic-Hydrothermal Ore Deposits. Econ. Geol. 100, 1287–1312. https://doi.org/10.2113/gsecongeo.100.7.1287

Figure Captions

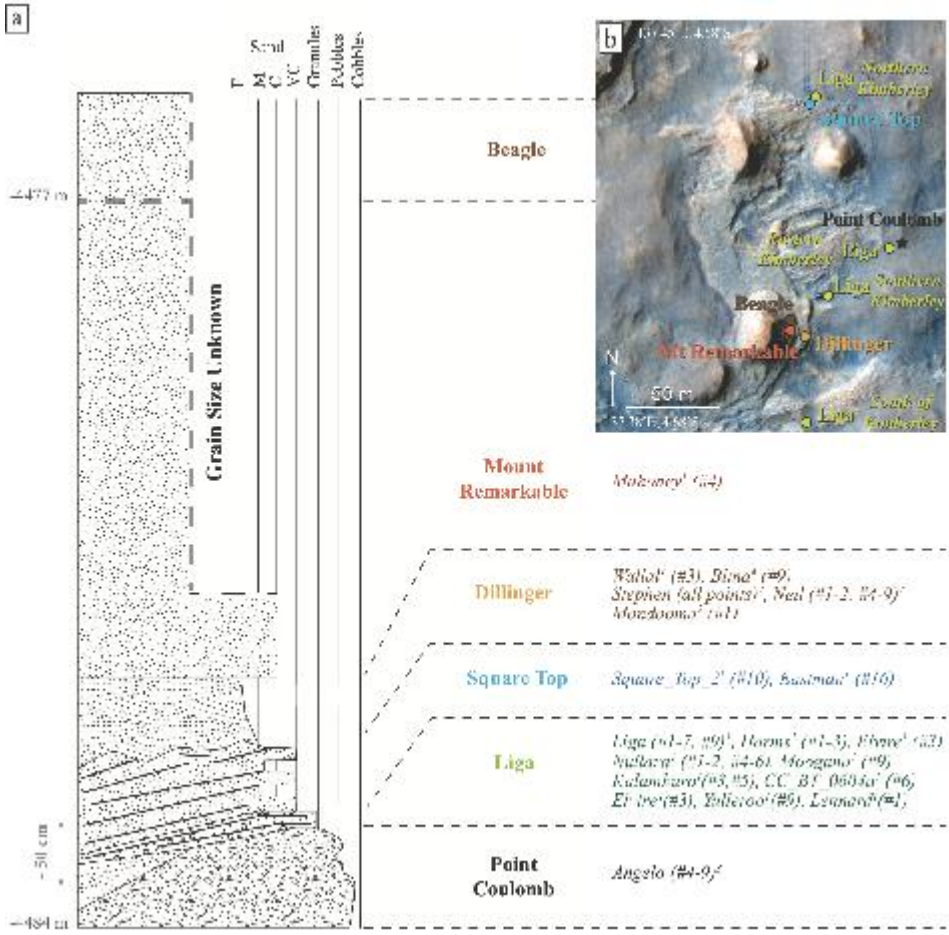

Figure 1. (a) Interpretative stratigraphic column of the Kimberley formation. The intersection of the units with the vertical lines indicates the grain sizes found in that unit. [1] corresponds to targets located on sedimentary bedrocks, [2] are targets located within fracture-fills, [3] are targets located on igneous rocks, and [4] are targets located on soil. Approximate elevation of the sedimentary column has been estimated by Stack et al. (2016). (b) HiRiSE image of the Kimberley formation presenting the location of the six Kimberley members.

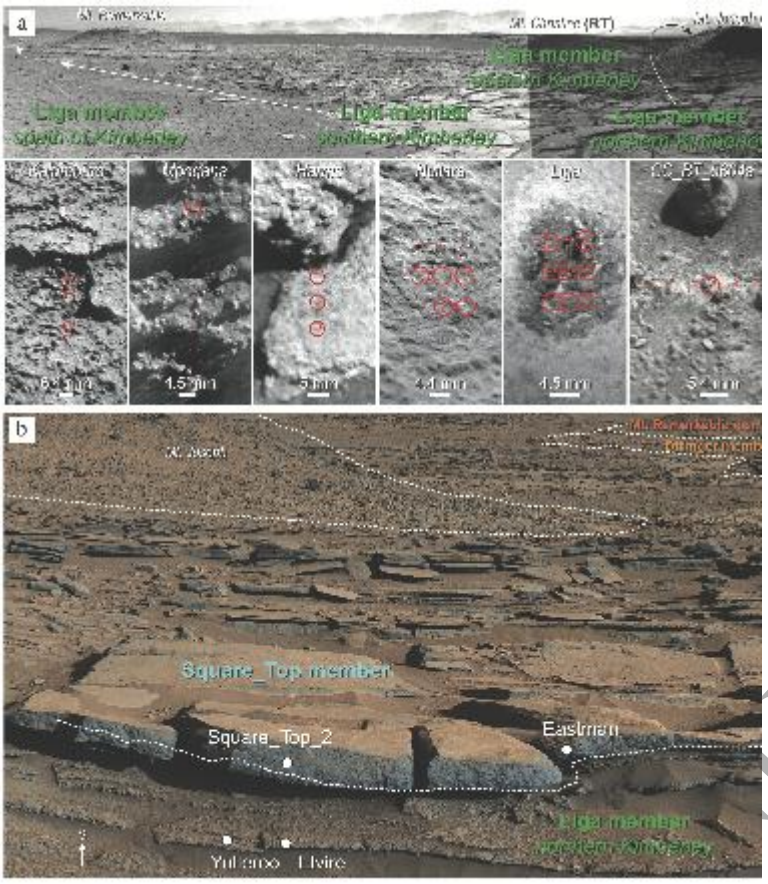

Figure 2. Facies of the North of Kimberley. (a) Navcam mosaic of Liga member modified from LeDeit et al. (2016) with RMI images of Kalumburo (sol 632), Moogana (sol 630), Liga, Harms and Nullara (sol 601), and CC_BT_0604a (sol 604). Red circles show the location of Cu-rich points in each target (Cu > 150 ppm). (b) Mastcam mosaic of the northern Liga and the Square Top member modified from Le Deit et al. (2016). White dots locate targets with at least one point containing elevated Cu values (> 150 ppm).

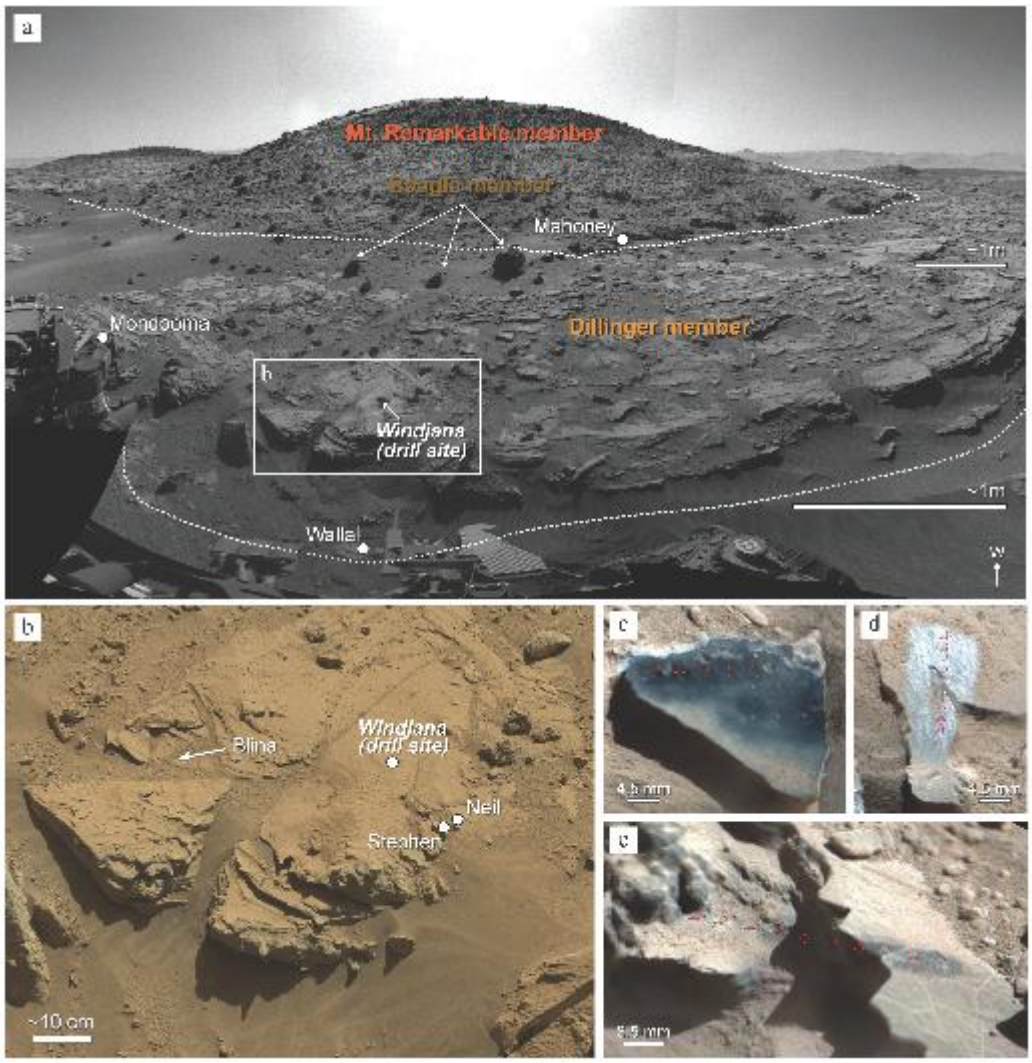

Figure 3. Facies of the uppermost (southern) part of the Kimberley formation. (a) Navcam mosaic of Dillinger and Mount Remarkable member modified from Le Deit et al. 2016). The Beagle member is at the top of the Mount Remarkable, and the dark blocks labelled « Beagle member » rolled downhill. (b) Mastcam mosaic of the Windjana drill site modified from LeDeit et al. (2016). The white dots and arrows present the location of targets with at least one point containing elevated Cu values (> 150 ppm). RMI images merged with Mastcam images of (c) Stephen (sols 611, 619 and 630), (d) Neil (sol 619) and (e) Mondooma (sol 625).

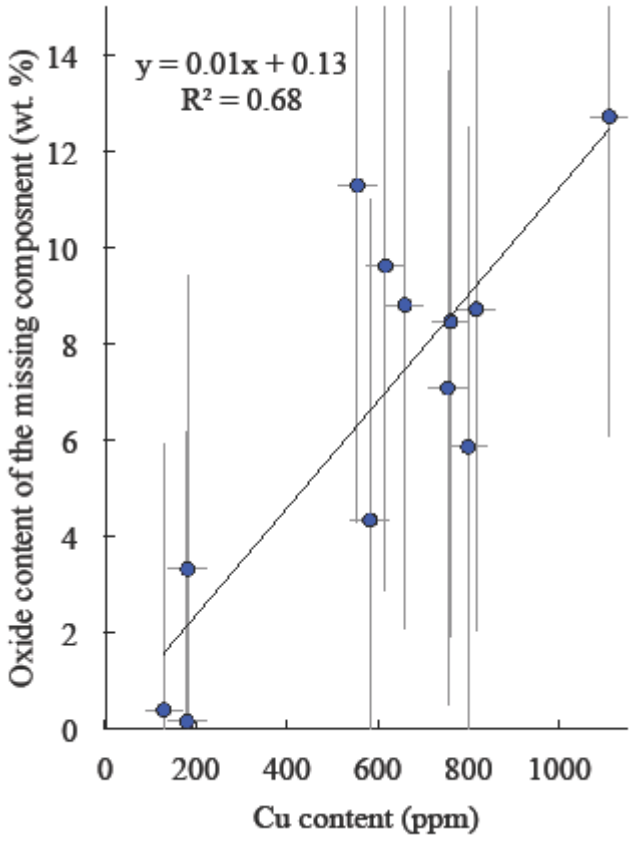

Figure 4. Figure 4. Cu content (ppm) versus the oxide content of the missing component(s) (wt. %) in CC_BT_0604a #6, Liga (#1-7, #9), Moogana #9 and Kalumburo #3 and 5. The x- and y-axis error bars represent the Cu accuracy (RMSE), i.e., +/- 41 ppm, and the accuracy of the missing component that is assumed to be equal to the accuracy of the total oxides, respectively.

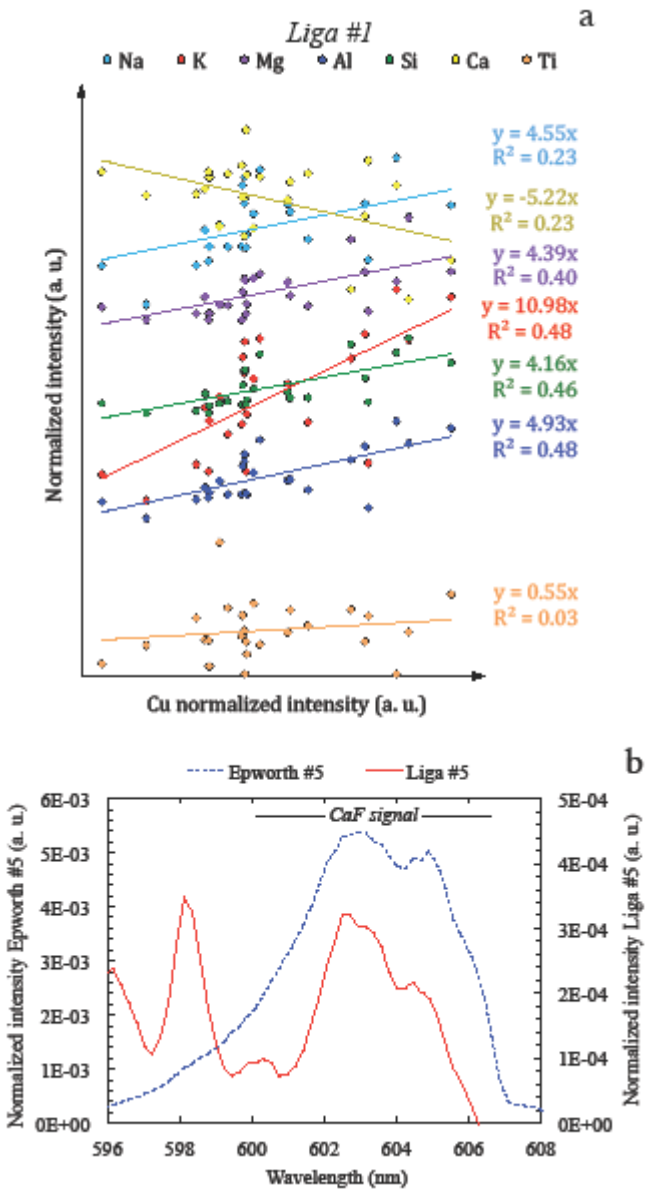

Figure 5. (a) Cu peak intensity variations variations versus elemental intensity trends without dust contribution in Liga #1. All shots contain >> 50 ppm of Cu. Only the slope of the linear regressions is indicated. (b) Spectral region of CaF molecular signal in Liga #5 (red line) compared to that of Epworth #5 (blue dashed line, sol 72) identified as fluorite by Forni et al. (2015), containing about 5.5 wt. % of F - one of the most intense F signal observed by ChemCam in Gale crater (Forni et al., 2015). The atomic line at 598.2 nm corresponds to Si II emission line.

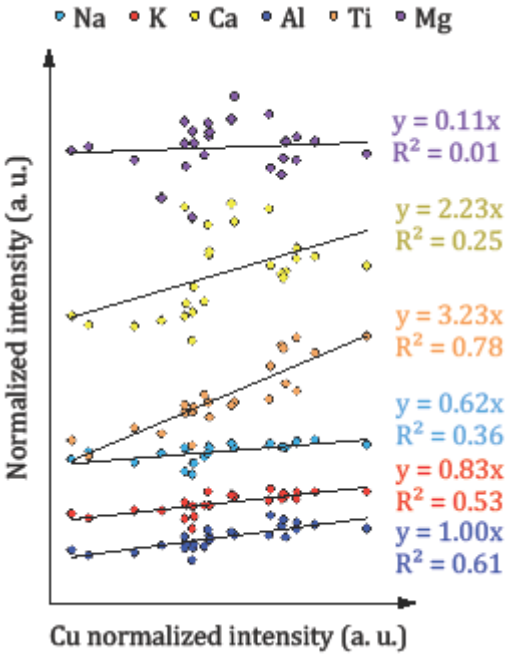

Figure 6. Cu peak intensity variations versus elemental intensity trends without dust contribution in CC_BT_0604a #6, found in the Liga member in the northern part of Kimberley. All shots contain >> 50 ppm of Cu. The units are in arbitrary unit (a. u.). Only the slope of the linear regressions is indicated.

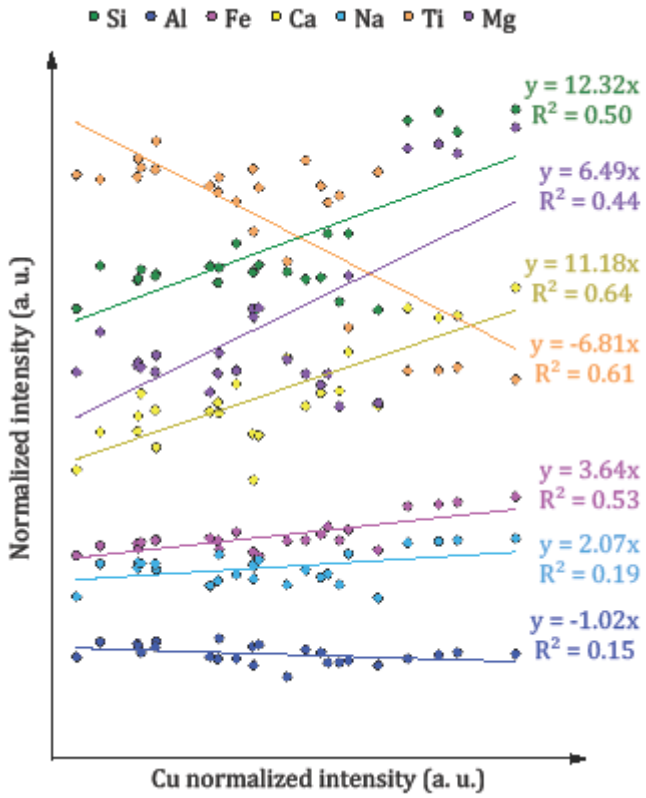

Figure 7. Cu peak intensity variations versus elemental intensity trends without dust contribution in Moogana #9. All shots contain >> 50 ppm of Cu. The units are in arbitrary unit (a. u.). Only the slope of the linear regressions is indicated.

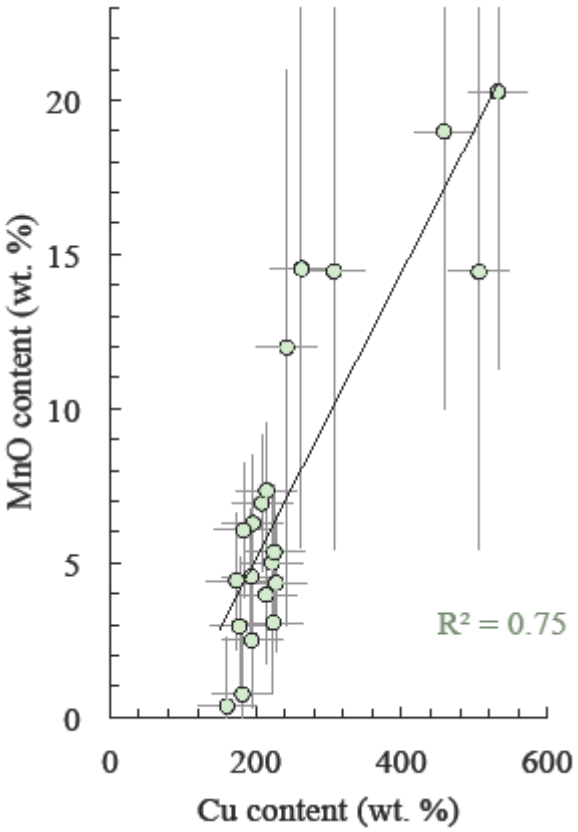

Figure 8. Copper concentration versus MnO contents for Cu-rich points of targets located on fracture-fills in the Dillinger member i.e., only Stephen, Stephen_DP, Neil and Mondooma targets. The x axis error bars represent the accuracy (RMSE) of Cu quantification, and the y axis error bars display the RMSE of MnO calibration (Lanza et al., 2016).

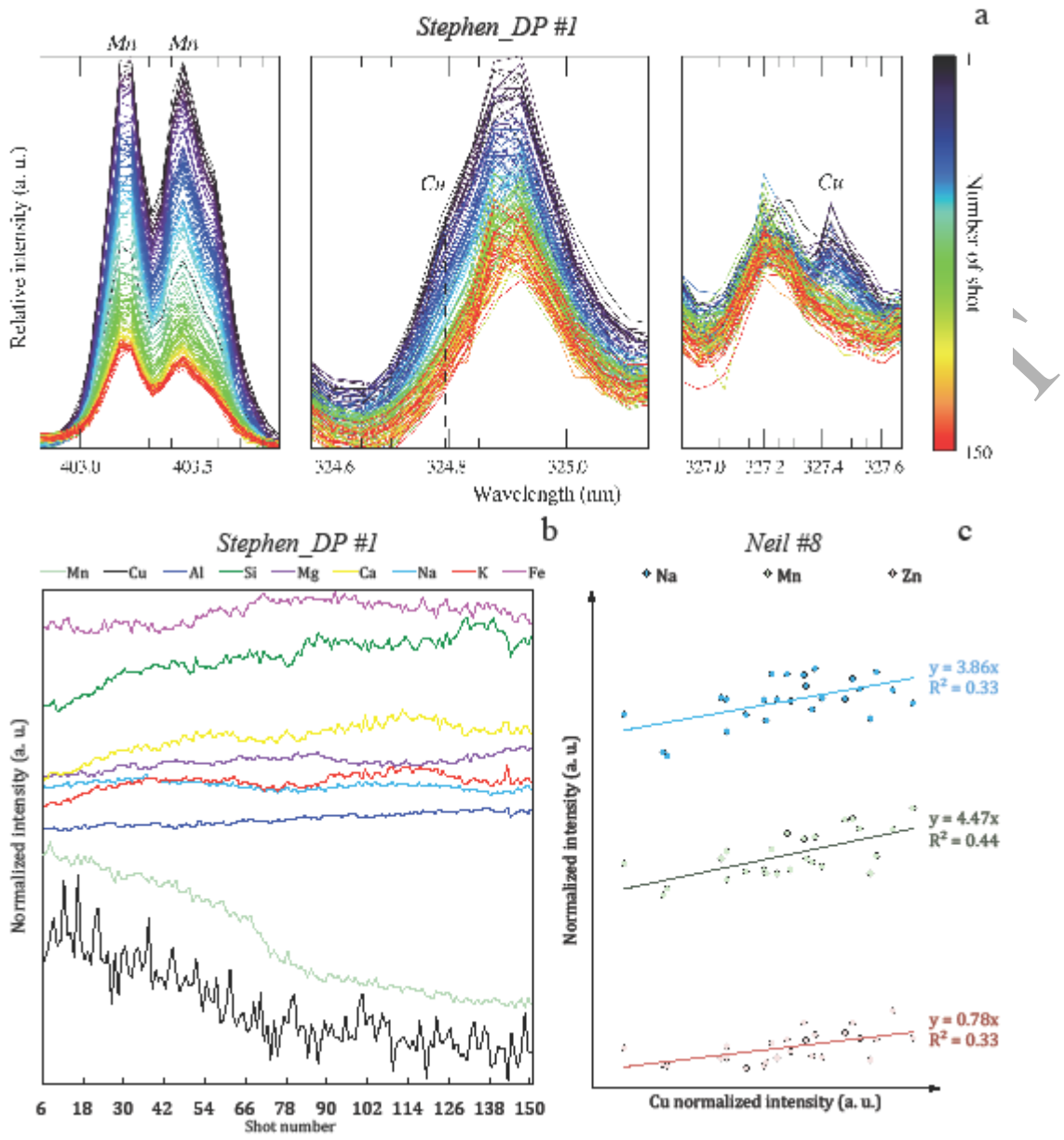

Figure 9. (a) Depth profile of Mn I 403.19 nm and Mn I 403.42 nm, and Cu I 324.786 nm and Cu I 327.429 nm in Stephen_DP #1. (b) Elemental peak intensity trends with depth of Cu (black curve), Mn (light green curve), Si (green curve), Al (dark blue curve), Fe (pink curve), Mg (purple curve), Ca (yellow curve), Na (light blue curve), and K (red curve) in Stephen_DP #1. (c) Cu peak intensity variations versus elemental intensity trends without dust contribution in Neil #8. All shots contain >> 50 ppm of Cu. The units are in arbitrary unit (a. u.). Only the slope of the linear regressions is indicated.

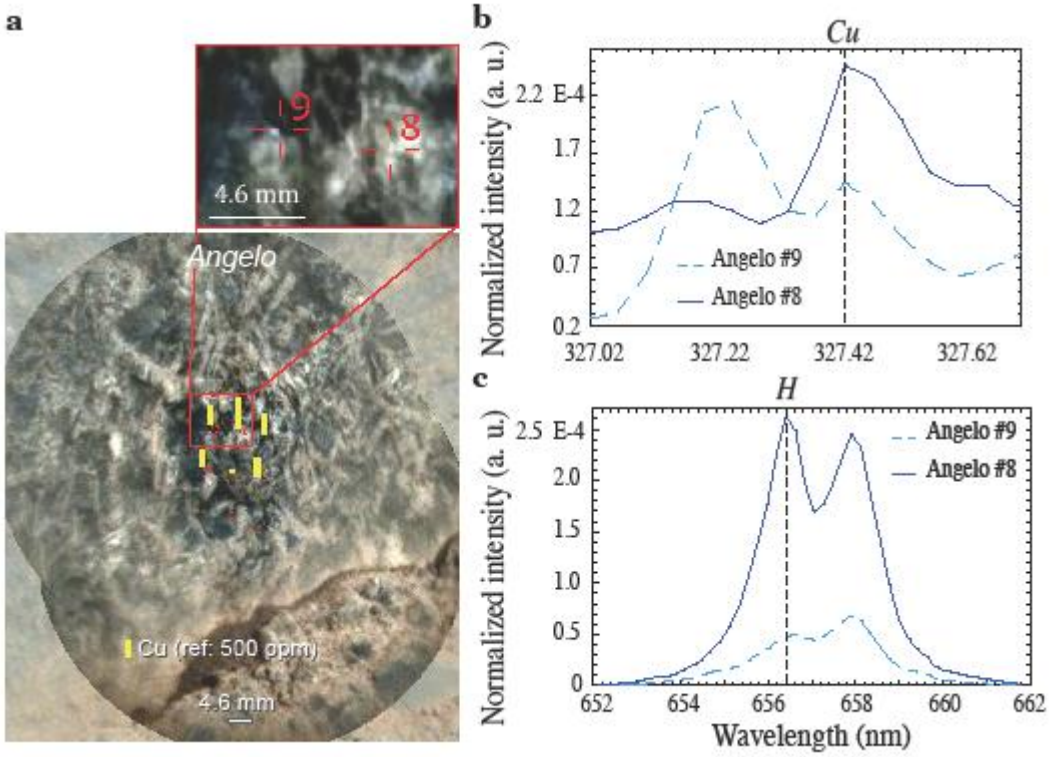

Figure 10. (a) RMI image merged with the Mastcam image of Angelo (sol 553) at Point Coulomb, with a zoom of point #8 and #9. The yellow bars show Cu content in each point. LIBS spectra of Angelo #8 (dark blue line) and #9 (light dashed blue line) around (b) Cu I at 327.428 nm spectral range (c) H I at 656.2 nm spectral range. The units are in arbitrary unit (a. u.).

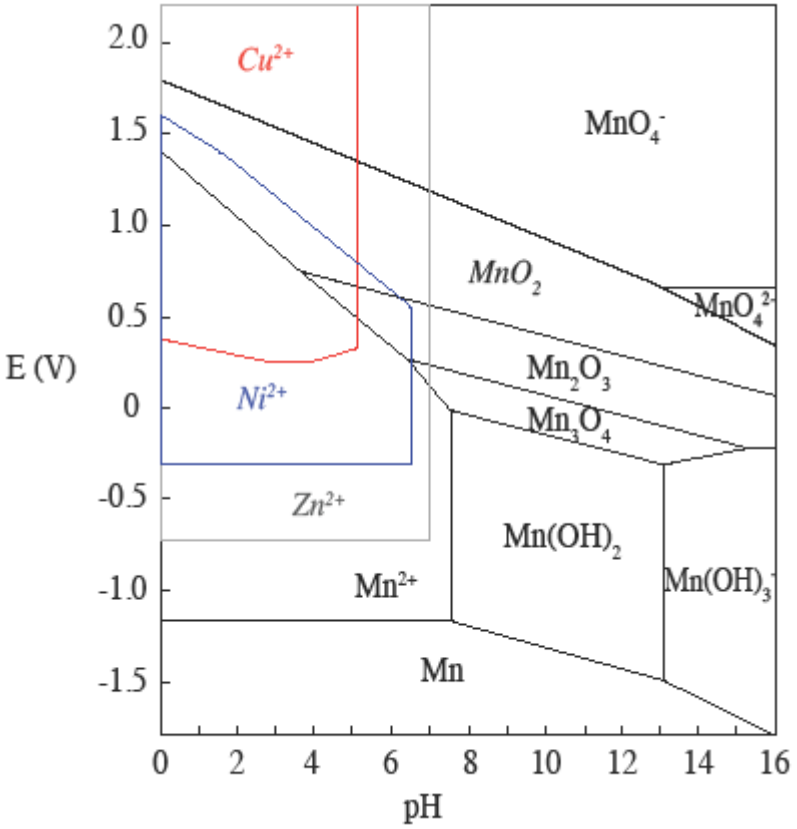

Figure 11. Potential (E in volt) – pH diagram for Mn-H_2O system at 1 bar and 25°C. The stability of Cu2+, Zn2+ and Ni2+ are also shown in red, gray and blue box respectively in a H_2O system at 1 bar and 25°C (Guilbert and Park, 2007).

Table 1. Oxide contents (wt. %) and Cu concentrations (ppm) within targets located at Kimberley with elevated copper amounts (>150 ppm)

	Sol	Target name	# Point	Sequence	Cu	SiO_2	TiO_2	Al_2O_3	FeOT	MgO	CaO	Na_2O	K_2O	MnO	ZnO	Total
Liga	574	Lennard	1	CCAM02 574	322	57.0	0.7	18.0	12.1	2.0	7.1	5.0	4.0	0.81	-	106.7
Northern Kimberley	578	Yulleroo	9	CCAM03 578	464	38.7	-	7.9	42.9	3.6	2.6	2.8	1.6	0.46	-	100.7
	581	Elvire	3	CCAM04 581	325	46.4	0.8	12.0	29.0	4.2	3.2	2.5	2.2	0.78	-	101.1
	604a	CC_BT_0	6	CCAM15 026	817	44.4	0.9	8.1	19.6	8.6	5.6	2.0	2.0	-	-	91.3
Liga	Liga	Liga	1	CCAM01 601	660	43.2	0.7	7.3	18.6	13.3	4.1	2.9	1.1	0.15	-	91.3
	Liga	Liga	2	CCAM01 601	755	44.3	0.8	7.3	17.5	16.6	3.5	2.2	0.9	0.15	-	93.1
	Liga	Liga	3	CCAM01 601	761	43.1	0.7	7.9	17.1	16.0	3.3	2.4	0.9	0.09	-	91.6
	Liga	Liga	4	CCAM01 601	799	44.7	0.7	6.9	17.3	16.7	4.6	2.3	0.9	0.13	-	94.3
Southern Kimberley	Liga	Liga	5	CCAM01 601	1110	42.1	1.7	7.1	19.4	7.4	4.8	1.6	3.2	0.02	-	87.3
	Liga	Liga	6	CCAM01 601	618	43.5	0.7	6.0	17.6	14.1	5.6	1.5	1.3	0.08	-	90.5
	Liga	Liga	7	CCAM01 601	583	49.4	0.6	6.4	16.0	13.7	6.4	2.0	1.3	0.12	-	95.8
	Liga	Liga	9	CCAM01 601	181	56.1	0.7	19.9	0.7	2.1	9.1	5.3	2.8	0.01	-	96.7

	60			CCAM02		48.				14.				0.0	-	95.
	1	Harms	1	601	524	8	0.7	6.2	16.6	3	5.2	2.8	0.7	7		3
	60			CCAM02		51.				13.				0.3	-	99.
	1	Harms	2	601	339	8	0.6	9.9	16.5	3	2.1	2.2	2.4	2		2
	60			CCAM02		51.				11.				0.1	-	99.
	1	Harms	3	601	638	3	0.6	10.5	16.1	6	3.6	3.8	1.5	2		2
	60			CCAM03		56.				10.				0.0	-	99.
	1	Nullara	1	601	283	0	0.8	10.4	11.9	7	3.0	2.5	4.0	9		4
	60			CCAM03		47.				12.				0.0	-	94.
	1	Nullara	2	601	383	6	0.6	7.3	16.6	1	6.8	2.5	1.0	8		8
	60			CCAM03		46.				14.				0.1	-	95.
	1	Nullara	4	601	331	3	0.7	6.7	18.2	6	4.2	3.3	1.1	4		1
	60			CCAM03		50.				14.				0.0	-	98.
	1	Nullara	5	601	285	1	0.7	8.6	16.1	0	3.8	2.6	2.1	9		1
	60			CCAM03		42.				14.				0.1	-	91.
	1	Nullara	6	601	398	5	0.6	4.1	19.6	9	6.9	2.3	0.4	8		5
	63			CCAM01		40.								0.3	-	89.
Liga	2	Moogana	9	632	556	0	0.7	5.9	23.9	9.4	5.5	1.8	1.5	3		0
	63	Kalumbur		CCAM02		63.							11.	0.0	-	99.
South of	2	o	3	632	130	1	0.2	19.7	0.7	0.9	2.1	1.4	4	3		6
Kimberl	63	Kalumbur		CCAM02		58.								0.0	-	99.
ey	2	o	5	632	180	1	0.7	18.1	5.5	1.4	4.7	5.1	6.3	6		9
		AVG			**497**	**48.2**	**0.7**	**9.7**	**16.9**	**10.2**	**4.7**	**2.7**	**2.4**	**0.20**		**95.8**
		STD			**247**	**6.4**	**0.2**	**4.7**	**8.5**	**5.4**	**1.8**	**1.1**	**2.4**	**0.22**		**4.7**
	57	Square_To		CCAM04		42.								1.0	-	99.
Square	8	p_2	10	578	699	8	0.8	7.6	35.0	3.7	3.5	2.6	2.8	0		8
Top	58	Eastman	16	CCAM02	625	39.	0.7	5.1	30.0	5.1	3.0	2.1	1.1	0.5	-	86.

	5			585		2							5		9
						41.							**0.7**		**93.**
			AVG		**662**	**0**	**0.7**	**6.4**	**32.5**	**4.4**	**3.3**	**2.4**	**2.0**	**8**		**4**
														0.3		
			STD		**53**	**2.6**	**0.1**	**1.8**	**3.5**	**1.0**	**0.3**	**0.4**	**1.2**	**2**		**8.8**
	60			CCAM04		46.								0.3		95.
Dillinger	8	Wallal	3	608	406	7	0.8	8.6	21.3	7.9	3.1	4.7	2.4	0	-	8
	61			CCAM04		45.								0.4		94.
	1	Blina	9	611	904	9	0.8	11.6	18.7	7.0	6.0	1.7	1.9	6	-	1
	61			*CCAM01*		*44.*								*6.9*	*0.6*	*94.*
	1	*Stephen*	*1*	*611*	*208*	*1*	*0.8*	*7.3*	*17.7*	*9.6*	*3.5*	*2.5*	*1.8*	*4*	*9*	*8*
	61			*CCAM01*		*39.*				*13.*				*18.*	-	*102*
	1	*Stephen*	*2*	*611*	*459*	*2*	*0.7*	*5.8*	*17.4*	*6*	*2.9*	*2.4*	*1.3*	*97*		*.2*
	61			*CCAM01*		*39.*				*14.*				*20.*	-	*103*
	1	*Stephen*	*3*	*611*	*532*	*1*	*0.7*	*5.5*	*17.9*	*2*	*3.1*	*1.7*	*1.2*	*26*		*.8*
	61			*CCAM01*		*43.*				*10.*				*7.3*	-	*94.*
	1	*Stephen*	*4*	*611*	*215*	*0*	*0.8*	*6.8*	*18.2*	*4*	*4.3*	*1.9*	*1.9*	*4*		*6*
	61			*CCAM01*		*38.*				*15.*				*14.*	-	*99.*
	1	*Stephen*	*5*	*611*	*263*	*9*	*0.7*	*5.5*	*18.2*	*6*	*3.1*	*1.7*	*1.2*	*54*		*4*
	61			*CCAM01*		*40.*				*13.*				*11.*	-	*97.*
	1	*Stephen*	*6*	*611*	*242*	*7*	*0.7*	*5.8*	*18.0*	*8*	*3.1*	*1.8*	*1.6*	*99*		*6*
	61			*CCAM01*		*46.*				*10.*				*0.3*	*0.6*	*91.*
	1	*Stephen*	*7*	*611*	*161*	*0*	*0.8*	*6.9*	*18.3*	*4*	*4.5*	*1.6*	*2.3*	*7*	*2*	*8*
	61			*CCAM01*		*40.*				*13.*				*0.7*	-	*87.*
	1	*Stephen*	*8*	*611*	*181*	*3*	*0.7*	*6.1*	*19.5*	*2*	*3.7*	*1.6*	*1.7*	*5*		*6*
	61			*CCAM01*		*38.*				*14.*				*4.4*	-	*90.*
	1	*Stephen*	*9*	*611*	*174*	*9*	*0.8*	*5.8*	*18.8*	*4*	*4.1*	*1.8*	*1.4*	*2*		*3*
	61			*CCAM06*		*37.*				*11.*					-	*83.*
	1	*Stephen*	*1*	*611*	*347*	*0*	*0.7*	*6.0*	*21.2*	*9*	*3.1*	*2.3*	*1.5*	-		*6*

61			CCAM06		38.				12.						85.
1	Stephen	2	611	290	9	0.7	6.5	19.9	9	3.2	2.1	1.6	-		9
61			CCAM06		41.				12.						86.
1	Stephen	3	611	326	1	0.7	7.0	18.2	3	3.6	1.9	1.8	-		6
61			CCAM06		43.				11.						87.
1	Stephen	4	611	251	4	0.7	7.2	16.9	3	3.9	1.9	2.0	-		2
61			CCAM06		43.				10.						86.
1	Stephen	5	611	226	8	0.7	6.7	16.5	7	4.3	1.9	2.1	-		5
61			CCAM06		43.				11.						85.
1	Stephen	6	611	332	1	0.7	5.7	16.6	1	4.1	1.7	2.1	-		0
61			CCAM06		41.				12.						85.
1	Stephen	7	611	291	3	0.7	5.6	17.8	9	4.0	1.5	1.5	-		4
61			CCAM06		43.				12.						87.
1	Stephen	8	611	467	0	0.7	6.0	17.4	5	4.1	1.6	1.7	-		0
61	Stephen_D		CCAM03		41.				13.				3.9		91.
9	P	1	619	214	4	0.7	7.1	16.9	9	4.5	1.7	1.6	7		7
61	Stephen_D		CCAM03		41.				15.				2.4		89.
9	P	2	619	195	1	0.7	6.5	16.6	3	4.1	1.6	1.5	9		8
61	Stephen_D		CCAM03		42.				12.						89.
9	P	3	619	152	9	0.6	7.5	17.4	0	4.4	2.1	2.0	-		0
61			CCAM04		39.				16.				2.9		88.
9	Neil	1	619	178	6	0.7	5.9	17.3	2	3.2	1.5	1.2	5		6
61			CCAM04		38.				14.				14.		97.
9	Neil	2	619	308	2	0.7	5.8	17.6	8	2.9	2.0	1.4	45		9
61			CCAM04		44.				10.				4.5	0.8	94.
9	Neil	4	619	194	4	0.8	7.1	18.2	8	4.0	1.8	1.8	6	6	2
61			CCAM04		42.				12.				3.0	0.8	92.
9	Neil	5	619	224	6	0.7	7.1	18.3	2	4.0	1.8	1.5	7	8	2
61			CCAM04		43.				10.				4.3		90.
9	Neil	6	619	228	2	0.8	6.0	18.3	2	3.6	1.8	2.5	5		7

61			*CCAM04*		*40.*				*13.*				*5.0*	*1.4*	*91.*
9	*Neil*	*7*	*619*	*222*	*2*	*0.7*	*5.9*	*18.8*	*3*	*3.4*	*1.9*	*1.1*	*0*	*7*	*9*
61			*CCAM04*		*40.*				*15.*				*6.2*	*0.7*	*93.*
9	*Neil*	*8*	*619*	*196*	*1*	*0.8*	*5.8*	*17.9*	*9*	*3.3*	*1.9*	*1.2*	*9*	*1*	*9*
61			*CCAM04*		*40.*				*13.*				*5.3*	*1.0*	*92.*
9	*Neil*	*9*	*619*	*226*	*3*	*0.8*	*5.9*	*19.2*	*8*	*3.3*	*1.8*	*1.0*	*5*	*7*	*6*
61			*CCAM04*		*39.*				*15.*				*6.0*		*91.*
9	*Neil*	*10*	*619*	*184*	*5*	*0.7*	*5.9*	*18.0*	*1*	*3.2*	*1.7*	*1.5*	*6*	-	*7*
62	*Mondoom*		*CCAM01*		*40.*				*13.*				*14.*	*1.6*	*104*
5	*a*	*1*	*625*	*506*	*9*	*0.8*	*6.7*	*18.3*	*8*	*3.3*	*3.0*	*1.6*	*44*	*7*	*.6*
					41.				**12.**				**6.9**		**93.**
	AVG			**291**	**5**	**0.7**	**6.6**	**18.2**	**6**	**3.7**	**2.0**	**1.6**	**3**		**8**
													5.9		
	STD			**152**	**2.4**	**0.0**	**1.2**	**1.1**	**2.2**	**0.6**	**0.6**	**0.4**	**2**		**5.4**
Mount Remarkable	615	Mahoney	4	CCAM02 615	358	47.7	0.8	11.2	20.1	8.8	4.7	1.6	4.5	0.31	-	99.7
Point Coulomb	553	Angelo	4	CCAM01 553	581	53.0	0.7	21.7	1.2	0.9	10.4	5.1	0.9	0.09	-	94.0
	553	Angelo	5	CCAM01 553	67	58.3	0.7	21.0	1.7	0.6	5.6	5.5	3.6	0.01	-	97.1
	553	Angelo	6	CCAM01 553	524	38.6	1.3	10.3	26.5	3.5	4.7	2.0	2.1	1.29	0.90	91.3
	553	Angelo	7	CCAM01 553	646	51.3	0.7	16.2	13.8	2.9	7.2	3.5	2.7	0.17	-	98.6
	553	Angelo	8	CCAM01 553	1005	54.8	0.7	18.2	5.2	1.5	7.6	4.4	2.4	0.02	-	94.7
	553	Angelo	9	CCAM01	574	37.	1.2	10.8	24.0	4.4	6.9	2.1	1.2	0.6	0.7	89.

3		553		8								7	8	7
				49.								**0.3**		**94.**
	AVG		**566**	**0**	**0.9**	**16.4**	**12.1**	**2.3**	**7.1**	**3.8**	**2.2**	**8**		**0**
												0.5		
	STD		**300**	**8.7**	**0.3**	**4.9**	**11.2**	**1.5**	**2.0**	**1.5**	**1.0**	**1**		**3.3**

For each point, Cu and major oxide concentrations are based on the averaged LIBS processed spectra without considering the five first spectra corresponding to the dust (Supplementary materials; Meslin et al., 2013; Wiens et al., 2013; Clegg et al., 2017).

'-' are values not quantified. Italic target names show ChemCam targets located in fracture fills.